This is a non-peer reviewed preprint.
This work was submitted to the Journal of Physical Oceanography on 22 January 2021.

Vertical fluxes conditioned on vorticity and strain reveal submesoscale ventilation

Dhruv Balwada*

School of Oceanography, University of Washington, Seattle, WA, USA

Qiyu Xiao

Courant Institute of Mathematical Sciences, New York University, New York, NY, USA

Shafer Smith

Courant Institute of Mathematical Sciences, New York University, New York, NY, USA

Ryan Abernathey

Lamont Doherty Earth Observatory, Columbia University, Palisades, NY, USA

Alison R. Gray

School of Oceanography, University of Washington, Seattle, WA, USA

**Corresponding author address:* Dhruv Balwada, School of Oceanography, 1503 NE Boat Street, Box 357940, Seattle, WA 98195-7940

E-mail: dbalwada@uw.edu

ABSTRACT

It has been hypothesized that submesoscale flows play an important role in the vertical transport of climatically important tracers, due to their strong associated vertical velocities. However, the multi-scale, non-linear and Lagrangian nature of transport makes it challenging to attribute proportions of the tracer fluxes to certain processes, scales, regions or flow features. Here we show that the surface vorticity and strain joint probability distribution function (JPDF) effectively decomposes the surface velocity field into distinguishable flow features like fronts and eddies. The JPDF has a distinct shape, which is at least partially determined by different flow instabilities. Further, this diagnostic approach approximately parses the flow into different scales, as stronger velocity gradients are usually associated with smaller scales. Conditioning the vertical tracer transport on the vorticity-strain JPDF can therefore help to attribute the transport to flow features and scales. Applied to a set of idealized Antarctic Circumpolar Current simulations that vary only in horizontal resolution, this diagnostic approach demonstrates that submesoscale fronts, despite their minuscule spatial footprint, play an outsized role in exchanging tracers across the mixed layer base and are an important contributor to the large scale tracer budgets.

1. Introduction

Accurate projections of future climate depend crucially on our ability to constrain and predict the magnitude, distribution, and efficiency of oceanic uptake of heat, oxygen, carbon and other important biogeochemical tracers. This tracer transport is influenced by flows at many scales. While the importance of mean flows and mesoscale eddies in transporting tracers has been recognized for many decades (Price et al. 1987; Marshall et al. 1993; Marshall 1997), recent evidence has suggested a significant contribution from submesoscale flows, which are thought to be particularly relevant for exchange across the mixed layer base (e.g. Ferrari 2011; Lévy et al. 2018; Mahadevan et al. 2020; Uchida et al. 2020).

Submesoscale flows are characterized by Rossby (*Ro*) and and Richardson (*Ri*) numbers that approach unity, and are associated with lateral scales roughly an order of magnitude smaller than the first internal deformation radius. This deviation from geostrophy allows strong vertical velocities to develop. They are usually more active near a boundary, and can emerge from instabilities of a mean horizontal buoyancy gradient (Boccaletti et al. 2007; Fox-Kemper et al. 2008; Callies et al. 2016), stirring by mesoscale eddies (Hoskins and Bretherton 1972; Lapeyre and Klein 2006; Roullet et al. 2012), or by interactions of fronts with surface forcing (Thomas et al. 2008). Regardless of the generation mechanism, these scales play a dominant role in setting the mixed layer properties (Su et al. 2018), and are thought to be key in transporting tracers across the mixed layer base (McWilliams 2016; Mahadevan 2016; Balwada et al. 2018; Klocker 2018; Bachman and Klocker 2020).

Observational evidence highlighting the strong vertical transport associated with individual submesoscale fronts has grown over the years (Omand et al. 2015; Adams et al. 2017; Olita et al. 2017; Ruiz et al. 2019; Archer et al. 2020; Siegelman et al. 2020), usually in the form of tracer filaments that are seen penetrating across the base of the mixed layer along an isopycnal or strong vertical velocities that extend far below the mixed layer base. However, observationally assessing the impact of these structures on regional and global scales remains challenging, due to a lack of statistical knowledge about their strength and frequency.

Modeling studies have suggested that resolving submesoscale flows quantitatively changes the tracer exchange across the mixed layer. Such models include those that simulate single flow features like fronts or eddies (Mahadevan and Tandon 2006; Ramachandran et al. 2014; Brannigan 2016; Freilich and Mahadevan 2019), as well as those using large domains that are many deformation radii in size and represent a large region of the ocean (Lévy et al. 2001; Balwada et al. 2018; Klocker 2018; Uchida et al. 2019; Bachman and Klocker 2020). However, even given the complete spatio-temporal simulated data provided by models, the attribution of the enhanced vertical transport to specific submesoscale processes, dynamics or scales is not straightforward.

The difficulty in attribution can be appreciated by considering the flow and tracer transport in the submesoscale-resolving simulation of Balwada et al. (2018, described in section 2a). The surface vorticity field clearly indicates the presence of submesoscale features like fronts and eddies, and a passive tracer that is introduced at the surface reaches the interior in filaments and curtains that correspond visually with these features (Figure 1a,b). This correspondence results from two factors [1]: the tracer is being injected into the interior in regions associated with the strong submesoscale filaments and fronts, and more importantly, once a tracer filament reaches sufficient depth, it gets stirred by the dominant horizontal flow associated with these features at that depth. It is important to note that the vertical velocity and tracer flux are highly variable: a snapshot of vertical velocity is largely dominated by high-frequency waves (Figure 1c), and the magnitudes of vertical flux in a

[1] Readers can also refer to the movies of the tracer field evolution in these simulations that are provided in the supplementary material of Balwada et al. (2018).

snapshot (Figure 1d,e) are two orders of magnitude larger than its respective spatial average (Figure 1f). These properties suggest that a certain degree of spatio-temporal averaging is required to elucidate the vertical transport process.

A number of different approaches have been used to attribute transport to flow features or scales. The simplest approaches include modeling only the feature of interest, like a front (Freilich and Mahadevan 2019), or to select subregions in a more complex simulation that can qualitatively associated with the feature of interest (Balwada et al. 2018; Klocker 2018) and then to estimate Eulerian averages over these features. The advantage is the simplicity, but the disadvantages are numerous: a wide variety of features and scales contribute over time, lateral advection can get entangled with vertical fluxes, and the features of interest might be advected into and out of the region. Estimating the cross-spectra of the vertical fluxes over a fixed region helps provide more insight by distinguishing the influence of different scales. For example, Balwada et al. (2018) showed that internal waves have a negligible impact on the tracer flux even though they are the dominant signal in the vertical velocity. However, this study also showed that vertical flux had a broadband signal, with a wide range of scales contributing comparably to the downward flux. This broadband signal can be partially understood by noting that phase information is lost when plotting power spectra and the spectra are spatially non-local (Armi and Flament 1985; Franks 2005): a sharp front has a broad band signal in a power spectrum, instead of a single peak, and the shape of this spectrum is not sufficient to know that it represents a sharp front. Further, spectra of Eulerian fields may suffer from Doppler shifting: a geostrophically balanced front being advected through a region by the mesoscale flow may have an imprint at the superinertial frequencies and suggest a lack of balance where none is present (Callies et al. 2020). Another approach is based on identifying coherent structures, and estimating statistics following these structures. The simplest identification methods define structures based on some simple criteria (e.g. Capet et al. 2008, used a threshold on the second derivative to define fronts), while the most complex determine the structures using algorithms derived rigorously from continuum mechanics and dynamical systems theory (Haller 2015). The flow field is essentially cleaved into regions that are identified as coherent structures, under a particular selection criteria, and everything else. However, it is often found that the regions *around but outside* the structure boundaries are actually the most important for transport (Abernathey and Haller 2018; Zhang et al. 2019). Furthermore, in the presence of high frequency motions (e.g. inetria-gravity waves), it is often hard to even identify mesoscale coherent structures (Sinha et al. 2019).

The objective of this work is to quantify the role of different flow features, such as fronts or eddies, in the vertical transport of tracers. Our approach is motivated by Shcherbina et al. (2013), and centers on viewing the flow statistically, using the joint probability distribution function (JPDF) of strain and vorticity. We find that different regions in the vorticity-strain space correspond to distinct flow features, and that estimating conditional averages of vertical flux in this vorticity-strain space allows us to distinguish the contribution of these different features. Moreover, we find that the extent of the vorticity-strain JPDF is scale-selective, allowing also for the identification of flux with features of different scales. This empirical technique allows averaging in a quasi-Lagrangian frame, since vorticity and strain evolve on much slower times scales than the advection time scale. This technique is much simpler to implement than some of the coherent structure detection methods, does not discard regions as not being part of a coherent structure, and, as mentioned, provides flow scale information without any parameter tuning.

This paper is organized as follows. In section 2 we briefly review the simulations that are analyzed here, and investigate the properties of the associated vorticity-strain JPDFs. We demonstrate that the vorticity-strain JPDF can be used isolate features, discuss how instabilities shape it, and consider in some detail the signature of fronts in vorticity-strain space. In section 3, we consider the vertical velocities and fluxes of a passive tracer, demonstrating that the additional flux at higher resolutions is associated primarily with small-scale fronts, and also to submesoscale-driven changes in properties of the large scale flows. We conclude and discuss further applications and questions in section 4.

2. Flow structures in vorticity-strain space

a. Model details

All the diagnostics and results presented in study are from the analysis of a series of simulations, using the MITgcm, first presented in Balwada et al. (2018). The model setup is that of a channel forced by winds and thermal restoring, fashioned to be a simplified and idealized version of the Antarctic Circumpolar Current. The model domain is 2000 km by 2000 km horizontally and 3 km deep, with a Gaussian ridge that spans the entire meridional extent of the domain, and is 1 km high (shallowest point in the domain is 2 km) and 150 km wide (standard deviation of 75 km). The model is set on a β-plane centered at 35°S, and through out the text, we use f to indicate the meridionally-dependent Coriolis frequency, and $f_0 = f(35°\text{S})$. The surface forcing consists of a sinusoidal zonal wind stress akin to an atmospheric jet, with a maximum in the center of the domain, and a linear temperature restoring at the surface. Three different horizontal resolutions are used: 20 km, 5 km and 1 km. The vertical grid is the same for all simulations, with 76 levels, 1m spacing near the surface and approximately 150m spacing near the bottom. The vertical diffusivity K is prescribed by the KPP scheme (Large et al. 1994). The vertical grid and numerics are the same as those in the LLC4320 simulations (e.g. Rocha et al. 2016).

After the model fields were spun up, a tracer was forced at the surface by restoring to a target value of 1 kg m^{-3} in the top 1 m grid cell, with a restoring time scale of 72 minutes, corresponding to a gas transfer velocity of 80cm/hr, similar to the gas transfer velocities observed under moderately high-wind conditions in the Southern Ocean. See Balwada et al. (2018) for more details on the model setup, spectral properties of the simulations, and an analysis of the influence of horizontal resolution on the tracer uptake.

The tracer is continually forced at the surface for one year, and the amount of the tracer in interior increases throughout this year. Most of the analysis in this study is done using snapshots of the flow field separated by 10 days, and spread over this year. After the tracer is switched on, it undergoes transient phase of about 2 months during which it is taken up by rapid diffusion into the mixed layer. During the period between months 3–12, the tracer concentration in the interior is increasing, but the fluxes themselves stay in relative equilibrium. Model output for the diffusive fluxes of tracers were only saved for the first 6 months of the simulation, which limits the analysis period that can be considered when analyzing tracer budgets. Therefore, in section 3b we use daily snap shots from months 3–6. However, none of the statistical results in this study are qualitative effected by these choices of the number and frequency of snapshots used, since we ensured that all the statistics evaluated are converged. Spatially, the analyzed region extends from $y = 500$km to $y = 1500$km (Figure 2a), which excludes regions adjacent to the northern and southern boundaries to ensure that unrealistic dynamics due to the presence of vertical walls do not influence the results.

b. Joint Probability Distribution Function (JPDF) of vorticity and strain

The analysis of two-dimensional flows in terms of the gradients of the velocity field (the strain tensor) is a fundamental tool with a long history. Okubo (1970) and Weiss (1991), for example, showed that the eigenvalues of the strain tensor could be used to understand the evolution of the gradient of a tracer advected by the flow. This serves as partial motivation for our investigation, with the acknowledgement that the surface flow can have significant deviations from a two-dimensional flow. This analysis is reviewed in Appendix A, and there it is also shown that the strain tensor can be expressed in terms of the the vertical vorticity, horizontal divergence, normal strain and shear strain. These are defined respectively as

$$\zeta = v_x - u_y, \quad \delta = u_x + v_y, \quad \sigma_n = u_x - v_y, \quad \text{and} \quad \sigma_s = u_x + v_y. \tag{1}$$

The normal and shear strains are not coordinate-invariant, however the vorticity, divergence, and strain magnitude

$$\sigma = \sqrt{\sigma_n^2 + \sigma_s^2} \tag{2}$$

are. Unless noted otherwise, the term 'strain' will correspond to the strain magnitude normalized by the absolute value of the Coriolis frequency $\sigma/|f_0|$, the 'vorticity' to the vorticity normalized by the Coriolis frequency ζ/f_0, and 'divergence' to the divergence normalized by the absolute value of the Coriolis frequency $\delta/|f_0|$.

Snapshots of vorticity, strain and tracer concentration at three resolutions presented in Figure 2 clearly show the presence of coherent features, with the visually prominent features becoming smaller in size and stronger in magnitude as resolution is increased. In fact, the visually identifiable flow features broadly correspond to distinct signatures in vorticity and strain: cyclones have a prominent high vorticity core and a weak imprint on strain, fronts are associated with high-vorticity and high-strain filaments, and so forth. The asymmetry in the vorticity field is also clear at higher resolutions: the vorticity map is composed of a broad but relatively weak negative vorticity soup punctuated with sharp and long positive vorticity filaments vortices. Furthermore, the imprint of these flow features on the tracer is clear even below the mixed layer.

The distinct signature of different flow features on vorticity, strain and tracer concentration suggests that a statistical approach may reveal more quantitative connections. Inspired by results presented in Shcherbina et al. (2013), we consider the joint probability distribution function (JPDF) of strain and vorticity,

$$P(\zeta,\sigma), \quad \text{where} \quad \iint P(\zeta,\sigma)\,\mathrm{d}\zeta\,\mathrm{d}\sigma = 1 \tag{3}$$

(see Appendix B for the details of its calculation for discrete ranges and finite data). The JPDF has a distinct shape (Figure 3); it is centered near the origin, extends along lines of $\sigma = |\zeta|$, and is skewed with a longer cyclonic tail. This shape is a robust feature, and has been previously noted in other numerical simulations (Shcherbina et al. 2013; Rocha et al. 2016), as well as in real oceanic flows (Shcherbina et al. 2013; Berta et al. 2020).

We decompose the regions of the JPDF into three parts, corresponding roughly to anticyclonic flows where vorticity is negative and smaller than the strain ($\zeta/f_0 < 0$ & $\sigma < |\zeta|$; labeled 'ACYC'), cyclonic flows where the vorticity is positive and smaller than the strain ($\zeta/f_0 > 0$ & $\sigma < |\zeta|$; labeled 'CYC'), and frontal flows where the magnitude of the vorticity is smaller than the strain ($\sigma \geq |\zeta|$; labeled 'FRONT'). The labels are suggestive, for example it should not be taken to imply that every feature in the FRONT region corresponds precisely to a front.

To demonstrate that these regions correspond to the features described, in Figure 4 we consider the flow in a sub-region of the 1 km simulation, delineated by the dashed square in Figure 2a. The flow here is composed of a large anticyclonic swirl, embedded with fronts and cyclones. The reliability of our ad hoc separation in parsing flow features is supported by plotting separately the vorticity in $x-y$ space corresponding to the CYC, ACYC and FRONT regions in Figure 4d,e,f. As expected, the panel corresponding to ACYC shows the presence of a large anticyclonic swirl, CYC shows the presence of small intense cyclones, and FRONT shows filamentary vorticity streaks that correspond to fronts.

In the next subsections, we seek to understand what shapes the JPDF, and what it reveals about the underlying flow.

c. Instabilities shape the vorticity-strain JPDF

Many facets of the distinctive shape of the JPDF can be understood in terms of the different instabilities that can occur: the extremities of the vorticity-strain JPDF are controlled by a balance between the turbulent cascade of gradients trying to expand the JPDF and the the instabilities associated with the strong gradients on the extremities stopping this expansion.

First we consider the kinematics of the flow, which allows us to identify regions in vorticity-strain space where tracer gradients will undergo rapid exponential growth. In the Lagrangian frame, tracer gradients evolve like $\exp(-\lambda_{\pm}t)$, where $\lambda_{\pm} = \frac{1}{2}(\delta \pm \sqrt{\Omega})$ are the eigenvalues of the strain matrix, and $\Omega = \sigma^2 - \zeta^2$ is the Okubo-Weiss parameter (see Appendix A). In the absence of divergence, regions with $\Omega > 0$ (corresponding to the area labelled FRONT) will result in exponential growth of tracer gradients, with growth rate $|\lambda_{-}|$, and this rate is enhanced in the presence of convergence ($\delta < 0$). Figure 6a shows that the conditional mean of $\lambda_{-}/|f_0|$ (negative growth rate normalized by the absolute value of the Coriolis frequency) conditioned on vorticity-strain increases rapidly above the $\Omega = 0$ line (a formal definition of mean values conditioned on the vorticity and strain is given in Appendix B). These regions of very rapidly increasing tracer gradients, particularly for active tracers like buoyancy, are associated with very fast flows and can result in secondary instabilities (e.g. a similar criterion is referred to result in ageostrophic anticyclonic instability, AAI, in McWilliams 2016; Bachman and Klocker 2020). The strength of the buoyancy gradients (Figure 6b) does not exactly follow the eigenvalues and is generally larger in regions of positive vorticity and large strain; there are other factors apart from the growth rate that will determine how strong the gradients are.

The extent and asymmetry of the JPDF along the vorticity axis can be understood by considering the sign of the Ertel PV, $q = (\boldsymbol{\omega} + f\hat{\boldsymbol{z}}) \cdot \nabla b$, where $\boldsymbol{\omega} = \nabla \times \boldsymbol{v}$ is the vorticity vector, f is the Coriolis frequency, b is the buoyancy. In the absence of flow curvature, the flow is unstable to either inertial or symmetric instability if $fq < 0$ (Hoskins 1974). Alternatively, the flow is unstable when the nondimensionalized Ertel PV is less than 0, i.e.

$$\Pi = \frac{q}{fN^2} = 1 + Ro - Ri^{-1} < 0, \tag{4}$$

where geostrophic balance is assumed to hold at leading order, $Ro = \zeta/f$, and $Ri = f^2N^2/|\nabla b|^2$, where $N^2 = \overline{b}_z$. For $Ri \gg 1$, the flow is subject to inertial instability if $Ro < -1$, which suggests that the JPDF should be limited on the anticyclonic side to values with $\zeta/f \geq -1$. For sufficiently small Ri, such that $Ri^{-1} > 1 + Ro$, symmetric instability is possible on the cyclonic side as well.

Recently Buckingham et al. (2020a,b) developed a general stability criterion that applies to flow with curvature as well. A key result is that, for small enough Ri, cyclonic flows should be more unstable than anticyclonic flows. The criterion for instability is analogous to the Hoskins criterion with f replaced by the absolute angular momentum L, or $Lq < 0$. The nondimensional form of the criterion, analogous to (4), is

$$\Phi = (1 + Cu)(1 + Ro) - (1 + Cu^2)Ri^{-1} < 0, \tag{5}$$

where $Cu = 2V/(fR)$ is the curvature number, with V being the geostrophic speed and R being the radius of curvature. Here we estimate the radius of curvature as (Theisel 1995)

$$R = \frac{(u^2 + v^2)^{3/2}}{u^2 v_x - v^2 u_y + uv(v_y - u_x)}.$$

Figure 6b,c shows the conditional mean of Π and Φ, respectively, conditioned on the vorticity and strain. Note that unlike panel a, which is an estimate of a sort of growth rate, panels b and c are regime diagrams, indicating instability where values are negative. Both panels show inertial instability on the anticyclonic side, and symmetric instability limiting the frontal region ($\Omega > 0$). Interestingly, the criterion that accounts for curvature, Φ, is strongly negative on the cyclonic side as well, which may offer an explanation for the limitation of cyclonic vortices with low strain. Strikingly, the points of the JPDF that lie along the line $\zeta/f_0 = \sigma/|f_0|$, corresponding to the downwelling side of fronts (discussed later), are associated with the most stable flow.

d. Signatures of fronts

Fronts are ubiquitous in the ocean and occupy the largest surface area in the simulations (Table 1). At these locations, the vertical velocities can coherently and adiabatically connect the mixed layer and the interior if the front is deep, thus making them central in our study. Here we describe the canonical structure of fronts and try to better understand how they map onto the vorticity-strain JPDF. To make the discussion more concrete, Figure 7 shows the structure of a relatively straight front found in the 1 km simulation. The panels are arranged with plots in x-y along the top row, as well as the JPDF for this feature, and plots along x-z in the bottom row.

Fronts are associated with regions of sharp gradient in density (governed only by temperature in our simulations) at the surface, representing the core of the front (Figure 7a). These outcrops of density emanate to depth below the front, and in deep fronts can provide an adiabatic conduit from the mixed layer to the interior (Figure 7e). The density gradient is likely in geostrophic balance with an along-front velocity, which is strongest near the surface and decays vertically (yellow contours in Figure 7e).

During the process of frontogenesis, when a background flow is causing the surface density gradient to increase, an ageostrophic secondary circulation develops with a tendency to restratify the front: upwelling on the lighter side and downwelling on the heavier side. Typical submesoscale fronts tend to be asymmetric, with stronger cyclonic vorticity, convergence, and vertical velocity on the downwelling side of the front (Thomas et al. 2008; Shcherbina et al. 2013; McWilliams 2016). This is apparent here in Figure 7b,f. The asymmetry arises due to the vorticity tendency,

$\partial_t \zeta = (f + \zeta)\partial_z w + \ldots$, having an asymmetric response to vortex stretching. The vortex stretching near the surface ($\partial_z w$) strengthens the cyclonic vorticity, and compression strengthens the anticyclonic vorticity, but when $Ro \sim O(1)$ this response is asymmetric. Additionally, inertial instability also limits the range of anticyclonic vorticity that can be sustained (discussed in section 2c).

Figure 7f shows a vertical slice of the vertical velocity w, in which it can be seen that the asymmetry in the front also changes the vertical structure of this secondary circulation. The downwelling velocity core has a slight tendency to track the isopycnals and broaden at depth, resulting in a downwelling signal extending from the cyclonic side of the front at the surface to directly below the core at depth. Note also the presence of a high-frequency component on the upwelling side of the front, which is due to the presence of inertia-gravity waves.

These downwelling velocities can be very strong, $10-100$ m/day, and have the potential to rapidly transport tracers to depth. We see signatures of this in Figure 7g,h, which shows that the tracer penetrates as filaments to a few 100 m over the course of two days. In the particular case considered here, the tracer filament is not always perfectly aligned with isopycnals, which highlights the three-dimensionality of the transport process, and is likely a result of along-front variations. The upwelling side of the front is also a site where deeper water is brought to the surface, as highlighted by tracer-free anomalies sliding upward along the front into the mixed layer.

Fronts are also regions of strong strain (Figure 7c), and generally have a strain magnitude that is greater than the vorticity (as shown empirically in the previous section). This can be explained by considering a straight front and a local coordinate system oriented such that the along-front velocity v points in the $\hat{\boldsymbol{y}}$-direction. Then y-derivatives vanish, and from (1) and (2)

$$\sigma^2 = \delta^2 + \zeta^2 > \zeta^2. \tag{6}$$

This suggests that in the vorticity-strain JPDF (Figure 7d) the front will lie around or above the $\sigma = |\zeta|$ lines, at a distance that is determined by the strength of the surface divergence.

In the Hoskins and Bretherton (1972) classical theory of frontogenesis, with scaling for the atmospheric mesoscale, the associated ageostrophic divergence is small compared to the jet's strain and vorticity. Barkan et al. (2019) has however revisited this problem using asymptotic theory appropriate to submesoscale frontogenesis in the ocean's well-mixed surface layer. He shows that when fronts are in turbulent thermal wind balance (TTWB Gula et al. 2014), with $Ro \sim O(1)$, the associated ageostrophic divergence scales like the vorticity and strain, i.e. $|\delta| \sim |\zeta| \sim \sigma$. Assuming $|\delta| \approx |\zeta|$ in (6), we'd expect

$$\sigma \approx \sqrt{2}|\zeta|, \tag{7}$$

describing points with a slope of $\sqrt{2}$. This may be considered a sort of upper bound to the frontal signal, and indeed Figures 3 and 7d show that the points cluster between lines with slope 1 and slope $\sqrt{2}$.

This oceanic regime, where the divergence is comparable in strength to strain and vorticity, is present in our simulation. The conditional mean divergence (Figure 8a) highlights the presence of rapid convergence at fronts. We also consider a 3D JPDF of strain-vorticity-divergence, presented as a series of slices at various values of divergence in Figure 8b. Surface flows with the strongest convergence and divergence, $\delta/|f_0| \sim O(1)$, lie almost exclusively in the FRONT region, in contrast to ACYC and CYC regions having strong convergence and divergence that cancel each other out in the mean. This exclusive association between fronts and the strongest surface convergence and divergence is suggestive that fronts might have an outstanding impact on vertical tracer fluxes. We confirm this hypothesis in section 3.

e. Scale dependence in vorticity-strain space

Regions of larger strain and vorticity are usually associated with smaller scales, a result of the forward cascade of enstrophy. Since, the smaller scales are not resolved in lower resolution simulations, we expect that the range of vorticity and strain values sampled will decrease with resolution. This is confirmed by comparing the JPDFs from the simulations at different resolutions. The upper row of Figure 5 shows the JPDFs of vorticity and strain for the 5 km and 20 km simulations. Superposed on each figure are the outer contours of the JPDFs from the higher-resolution simulations, making it clear that the extent of the JPDF shrinks in size as resolution is lowered.

An alternative way to compare across scales is to use a coarse-graining filter on the highest resolution simulation. We specifically define a scalar field coarse-grained to grid-scale h as

$$\langle F\rangle^h(x_i,y_j) \doteq h^{-2}\int_{x_i-h/2}^{x_i+h/2}\int_{y_j-h/2}^{y_j+h/2} F(x,y)\,\mathrm{d}x\,\mathrm{d}y. \tag{8}$$

The coarse-grained vorticity is computed using the coarse-grained velocities as $\zeta^h \doteq \partial_x\langle v\rangle^h - \partial_y\langle u\rangle^h$, and analogously for the coarse-grained strain σ^h. This makes sense, since we want to compare the coarse-grained flow field to the flow field from a lower resolution simulation.

The bottom row of Figure 5 shows the JPDFs of vorticity and strain for the 1 km simulation, coarse-grained to 5 km (panel c) and 20 km (panel d). Remarkably, we see that the coarse-graining procedure shrinks the extent of the JPDF to almost exactly the contours for the lower resolution simulations. We tried a few different filtering techniques, and found that this qualitative result holds regardless of the exact methodology. This tells us that as resolution is increased and more submesoscale activity is admitted, the associated high strain and vorticity values come from features that are too small to resolve at lower resolution. Therefore, level-set contours of the JPDF of vorticity and strain can also be used as proxy for contours of lateral scales of flow features.

We use these ideas to segment the JPDF, and consequently the surface flow, beyond the three categories of fronts, cyclones and anticyclones. We subdivide the region from the 1 km simulation into a part of the JPDF that is contained inside the extent of the JPDF of the 5 km resolution simulation, and the part outside it (Figure 3). For the FRONT region these parts will be referred to as 'LARGE FRONT' and 'SMALL FRONT', respectively.

It is important to note that areas in the JPDF do not correspond to areas in x-y space (the areal extents of the various regions for each simulation are shown in Table 1). Because the peak of the JPDF is centered near the origin in vorticity-strain space, and the probabilities drop off very rapidly (notice the logarithmic color axis on Figure 3), the portion of the 1 km JPDF that lies within the 5 km simulation JPDF extent corresponds to about 99% of the spatial area. Moreover, while the full FRONT region of the 1 km simulation corresponds to 60% of the spatial area, the SMALL FRONT region represents less than 1% of surface area. The sharper flow features resolved only at higher resolution occupy very small spatial regions, but as shown in the next section have an out-sized impact on transport.

3. Vertical velocities and tracer transport in vorticity-strain space

Here we turn to the main theme of the paper: how to best determine what structures are responsible for the increase in vertical tracer exchange as resolution is increased. Having established in the previous sections how flow structures and scale are revealed in vorticity-strain space, we now consider vertical transport in this frame. We first consider vertical velocities conditioned on vorticity and strain, and then go on to study the impact of these flow features (regions of vorticity-strain space) on the transport of a tracer that is restored at the surface.

a. Vertical velocities

The conditional mean of vertical velocity, Figure 9, shows a pattern that is reminiscent of the conditional mean of surface divergence. Here we averaged over 30 time snapshots of model output, taken every 10 days (months 3-12). However, this pattern is very robust, and emerges qualitatively even if a single snapshot is used. This suggests that the degree of spatial averaging that is implicit when estimating averages conditioned on vorticity and strain is sufficient to filter out the high-frequency wave field that dominates a spatial map of vertical velocity (as seen in Figure 1c), and provides a robust method to obtain the signal that is relevant for transport.

The conditional mean vertical velocities in cyclonic and anticyclonic regions are similar across resolutions — anticyclones upwell in the mixed layer and downwell below the mixed layer, while cyclones do the opposite, with downwelling near the surface and upwelling deeper down. The frontal regions for the two lower resolution simulations are similar, with downwelling on the cyclonic side and upwelling on the anticyclonic side, and this pattern does not vary significantly down to a few 100 m below the mixed layer. This suggests that the fronts at these resolutions are relatively symmetric, and easily reach below the mixed layer base. In contrast, the frontal region in the 1 km simulation is far from being symmetric and shows significant changes with depth. Most of the frontal region is characterized by downward velocities, with the upward velocities present only very close to the $\zeta/f_0 = -\sigma/|f_0|$ line. It is notable that this region of upwelling does not extend to stronger anticyclonic vorticities, beyond $\zeta/f_0 \approx -1$, except right near the surface. Also, the strongest downwelling is in regions farther away from the $\zeta/f_0 = \sigma/|f_0|$ line, where the instabilities and the surface divergence are strongest (contrast to Figure 6).

Why do we find downwelling on the warm, anticyclonic side of the front (the FRONT region where vorticity is negative), and why does this occur only at the highest resolution? This can be explained by contrasting the secondary circulation associated with 2D frontogenesis in the quasi-geostrophic (QG) vs. semi-geostrophic (SG) equations (compare figures 1.8 and 1.9 in Shakespeare 2015). QG frontogenesis is symmetric, and even as the front steepens in time, the vertical velocities only change sign across the core of the front at all depths. In contrast, SG frontogenesis is not symmetric: the cyclonic side of the front sharpens rapidly, and the region of downwelling velocity, which is concentrated and strong on this cyclonic side near the surface, decreases in strength but widens laterally at depth to occupy part of the region that is under the warm/anticyclonic side of the frontal core. The frontogenesis at the lower resolutions, characterized by lower *Ro* and higher *Ri*, is bound to be more akin to QG dynamics, while at the 1 km resolution the frontogenesis is better-described by SG dynamics.

b. Vertical tracer transport

Having considered how vertical velocities vary in different flow features, we now study how the different flow features work in unison to transport a tracer from the surface into the interior. The tracer, C, in a control volume bounded horizontally over a geographical area and vertically from the sea floor to an arbitrary fixed depth (z) evolves according to the equation

$$\partial_t \langle C \rangle^z = -\overline{wC} + \overline{K\partial_z C} + \overline{F}\delta(z), \tag{9}$$

where $\overline{(.)}$ is the horizontal spatial mean at constant z (refer to Appendix B), $\langle C \rangle^z = \int_{-H}^{z} \overline{C}\,\mathrm{d}z'$ is the total amount of tracer in the control volume divided by the horizontal domain area A, and $\delta(z)$ is the Dirac delta function that is non-zero only at the surface. The total amount of tracer below a given depth can increase due to the advective flux ($-\overline{wC}$), diffusive flux ($\overline{K\partial_z C}$, where K is prescribed by the KPP scheme and changes as a function of the flow) or surface flux (which is either zero, or $\overline{F}$ if the control volume extends all the way to the surface). The horizontal fluxes are ignored because they are small over the chosen domain (shown in Balwada et al. 2018), since there are are no lateral gradients in tracer restoring.

In the mixed layer, both the advective and diffusive fluxes contribute, while below the mixed layer only the advective flux is non-zero. Balwada et al. (2018) found that during the initial few months of tracer forcing, the mixed layers are rapidly saturated with tracer, after which a quasi-steady state is achieved. During this quasi-steady state, the surface flux does not change much, i.e. $\partial_t \langle C \rangle^0 = \overline{F}$ is approximately constant, and thus even below the mixed layer, where the diffusive flux is zero, the rate of tracer change, $\partial_t \langle C \rangle^z = -\overline{wC} \approx \overline{F}$, is thus also approximately constant. The analysis presented here is for this phase of the tracer simulation.

1) Mean tracer fluxes conditioned on vorticity and strain

The mean fluxes conditioned on vorticity and strain, denoted $\overline{(.)}^{\zeta\sigma}$ (see Appendix B), shows that each flux term is impacted by the different flow features in very different ways (Figure 10). The conditional mean of the vertical advective tracer flux, $\overline{wC}^{\zeta\sigma}$, near the base of the mixed layer (Figure 10a) is large and downward in the regions of rapid downwelling associated with fronts, and upwards in regions of upwelling. In fact, it closely resembles the conditional mean of vertical velocities (compare to Figure 9b), and makes it clear that small-scale fronts play a significant role in the vertical advective transport of tracers.

What does it mean to have upward advective tracer flux, when the tracer source is at the surface and the tracer is being fluxed downward by design? This can be understood by considering two things. First, since the tracer concentration is always positive, $C \geq 0$, regions of upwelling will necessarily have a positive flux, and only the spatial mean over the horizontal domain $\overline{wC}$ need be downward (negative). Secondly, even if the flux is upwards, it does not imply that it will lead to an increase in tracer concentration above the depth level under consideration: the upward flux typically brings up waters with negative tracer anomalies (the concentration at depth is usually smaller than that in the shallower region).

An alternate way to consider the advective flux is to consider its Reynold's decomposition

$$wC = \overline{w}\overline{C} + \overline{w}C' + w'\overline{C} + w'C', \tag{10}$$

where the eddy terms are defined relative to the spatial mean, as $C'(x,y) = C(x,y) - \overline{C}$. The vertical advective flux is composed of four components, where the second and third vanish when integrating over the domain, and the first term is negligible because the mean vertical velocity is very small. The last term, the vertical eddy flux, dominates the spatial mean of the advective flux, and is negative (downward) almost everywhere in vorticity-strain space (Figure 10b). The difference between the total and eddy advective fluxes results from the third term ($w'\overline{C}$, not shown), which dominates the pattern of the conditional mean of the advective flux and has a similar pattern to the conditional mean vertical velocity (Figure 9) but will make no contribution to the spatial mean of the flux.

The transit of the tracer from the atmosphere to the ocean interior starts at the surface and proceeds through the mixed layer, so it is worth considering whether the different flow features can impact the surface and diffusive fluxes. The conditional mean of the surface flux is generally highest in regions of surface divergence (Figure 10c), usually associated with the upwelling side of fronts and anticyclones. These are the regions where deeper low-tracer waters are pulled up to the surface, creating the strongest mixed layer tracer anomalies and thus the largest surface flux from a restoring condition. The surface flux is also large in regions of strong downwelling associated with fronts (around $0 < \zeta/f_0 < 2$, compare to figure 8b). These regions do not have the largest vorticity and strain, but are associated with regions of the strongest surface convergence. The variations of the conditional mean of the diffusive flux are similar to that for the surface flux

(Figure 10d). The only difference is on the upwelling side of the fronts, where the diffusive fluxes tend to be relatively weaker. This is likely a result of the upwelling bringing deeper stratified waters into the mixed layer, which then suppresses the mixing by KPP on the upwelling side of the fronts.

2) The role of flow features in controlling the tracer fluxes

The conditional means considered above help understand the relative roles played by different flow features, on average and in isolation. To understand the net contribution of the flow features on tracer transport, we must also consider the conditional mean of the fluxes in different flow features along with the frequency of occurrence (via the JPDF) of different flow features. For example, the net contribution of advective flux as a function of vorticity and strain is $\overline{wC}^{\zeta\sigma} P(\zeta,\sigma)$, which when integrated over the whole vorticity-strain space gives the spatial mean of the advective flux, $\overline{wC} = \iint_R \overline{wC}^{\zeta\sigma} P(\zeta,\sigma)\, \mathrm{d}\zeta\, \mathrm{d}\sigma$.

The conditional mean of each flux component shows variations across features, but the variations are much smaller for the surface and diffusive fluxes as compared to the advective flux — notice the colorbars are logarithmic in Figure 10a,b and linear in Figure 10c,d. This results in the net impact of the surface and diffusive fluxes having variations across the vorticity-strain space that are set primarily by the JPDF (Figure 11c,d).

However, the conditional mean of advective fluxes varies by orders of magnitude across the vorticity-strain space, and its sum in different parts of the vorticity-strain space is not simply a function of the spatial surface area occupied by that part (Figure 11a,b). This highlights the significant role played by finer-scale features in the vertical advective transport of tracers. It is particularly noteworthy that this relatively higher contribution at the finest scales is primarily limited to fronts — compare the total and eddy advective flux on the periphery of the JPDF in the FRONT region to the ACYC and CYC regions (Figure 11a,b).

3) Depth dependence of the contribution of different flow features to tracer fluxes

In Figure 12 we investigate the depth dependence of the contribution from the different flux components, integrated over regions of the vorticity-strain JPDF, for the 1 km and 5 km resolution simulations. The surface flux matches the diffusive flux at the surface (Figure 12b,e), since the advective flux is zero here, and the contributions from the different flow features is largely governed by the spatial area occupied by them (Table 1).

The advective fluxes (Figure 12a,d) are largest in the mixed layer, where a large cancellation between the fronts and anticyclones takes place, while the contribution from cyclones is relatively weak. The contribution from the anticyclones rapidly diminishes below the base of the mixed layer, while the frontal contribution penetrates much deeper. This results in the sum of the advective fluxes peaking at the base of the mixed layer, and being primarily dominated by the frontal regions at depths below the base of the mixed layer. Correspondingly, the eddy advective flux (Figure 12c,f) peaks at the base of the mixed layer and has the largest contribution from the frontal region, with the anticyclones and cyclones having a much smaller contribution and a weak depth dependence.

To compare the fronts between the 1 km and 5 km simulations, we separate the frontal region into 'LARGE FRONT' and 'SMALL FRONT' regions, as described at the end of section 2e. The large front contributes more than the small fronts to the tracer flux, but they also occupies a much larger spatial area than that for the small front region (Table 1). The contribution from the small fronts decreases below the base of the mixed layer. This suggests that the enhanced tracer flux at higher resolutions is not simply a result of additional smaller scales being resolved, but also due to the contribution by the larger scales increasing, as also shown in Balwada et al. (2018) and Uchida et al. (2019) using spectral decompositions.

4) Net contribution to tracer flux by different lateral scales

The highest probability, the peak of the JPDF $P(\zeta,\sigma)$, is near the origin and corresponds to vorticity and strain values at the largest scales, resolvable at all resolutions. The probability decreases as we move from the origin to higher vorticity and strain values, which correspond to smaller scales and require higher resolutions to be resolved (also see discussion in Section e). We form a new axis, $P_{\max}/P$, that takes a value of one at the largest probability ($P_{\max}$) near the origin and extends to larger values outwards from the origin. The properties at a particular value of $P_{\max}/P$ correspond to an integral along level sets of probability (contours of the JPDF).

The different flux components add up at different rates as $P_{\max}/P$ increases, as shown for the 1 km simulation in Figure 13a. As discussed above, the surface and diffusive fluxes are relatively homogeneous compared to the advective fluxes, and asymptote to their total contributions at a rate that is set largely by how much spatial area is contained inside each $P_{\max}/P$ contour. This can be seen convincingly when comparing the area fraction to the flux fraction inside each $P_{\max}/P$ (Figure 13b).

In contrast, the eddy advective flux asymptotes much more slowly, clearly indicating that smaller scales — the points on the periphery of the JPDF, with larger $P_{\max}/P$ — play an outsized role. For example, the region outside $P_{\max}/P = 10$ contains 20% of the area but more than 55% of the flux, while the region outside $P_{\max}/P = 100$ contains contains less than 5% of the area but 20% of the flux.

We also use $P_{\max}/P$ from the 1 km simulation to compare the vertical advective fluxes across resolutions and also against the coarse-grained fields from the 1 km simulation (Figure 14a,b), comparing the role played by the vorticity-strain values that are resolvable at the lower resolutions and the additional contributions coming from the values that are not resolved. The advective flux first increases and then rapidly decreases as $P_{\max}/P$ increases, suggesting a net downward flux. The upward signal at lower $P_{\max}/P$ is a result of the strong upwelling in the anticyclones and cyclones that is present closer to the peak of the JPDF, and is much stronger at 1 km resolution than at lower resolutions. When considering only the eddy advective flux, we do not see this upwelling signal at smaller $P_{\max}/P$, which is consistent with Figures 10b and 11b.

The difference between the simulations versus the coarsened fields is not very dramatic. This analysis helps re-emphasize the role played by smaller scales, which are unresolvable on coarser grids and occupy a very small fraction of the surface area, in fluxing tracer to depth. At the lower resolutions, changing from 20 km to 5 km, the additional flux is a result of simply resolving a wider range of vorticity-strain values. At 1 km resolution, the flux even at the lower vorticity-strain values is modified — this is in agreement with the dynamics of the fronts changing from being QG-like to SG-like as resolution increases.

4. Discussion

Here we have demonstrated that surface vorticity-strain JPDFs are a powerful analytical tool that can easily distinguish different flow features, and help study the impact of these flow features by providing a convenient frame to perform conditional averages. We showed that the peculiar shape of the JPDF, which has been noted previously in observations (eg. Shcherbina et al. 2013; Berta et al. 2020), is shaped in part by flow instabilities. Conditioning vertical velocities and vertical advective tracer fluxes on strain and vorticity helped highlight the outsized impact played by smaller-scale flow features, particularly fronts, in the vertical exchange of a tracer across the base of the mixed layer: $\sim 20\%$ of the vertical flux is achieved in fronts that occupy less than $\sim 5\%$ of the surface area.

This study has helped address an obvious question that has arisen from observational campaigns centered around individual fronts (Shcherbina et al. 2013; Mahadevan et al. 2020) — even though fronts are observed to be sites of significantly enhanced transport, are they frequent enough to play an important role in setting the large scale tracer budgets? We have convincingly shown here that submesoscale fronts do end up playing an important role on the net transport, and more emphasis needs to be placed on their parameterization, particularly their role in exchange between the mixed layer and the interior (Fox-Kemper et al. 2008; Uchida et al. 2020; Bachman and Klocker 2020).

One of the caveats of our study is that we condition the flux at depth on the surface properties. It is possible that some features at depth may not be directly related to the surface vorticity-strain, but rather to only the part of the surface horizontal flows that have not decayed at that level; generally smaller features decay more rapidly with depth than larger features. More analysis is needed to assess how important this effect is, and it will be part of future work. A counter-argument is that it is important to condition on surface properties, because that is the region that interacts with the atmosphere and supplies tracers to depth (or allows for outgassing of tracers leaving the ocean). So even if a number of small fronts decay and merge to form a single weaker front at depth, the transport in this deeper front would depend critically on how much tracer reaches it via the smaller fronts.

Our highest resolution simulations are at 1 km, which is sufficient to resolve the interior baroclinic instability, the fronts that form at the surface due to the associated mesoscale eddies, and to some degree even the mixed layer instabilities (Balwada et al. 2018; Uchida et al. 2019). We likely do not resolve the full impact of smaller submesoscale dynamics or instabilities, e.g. symmetric instability, which are suggested to enhance vertical transport across the mixed layer even further (Brannigan 2016; Smith et al. 2016). Regardless, it is very likely that fully resolving the submesoscale will enhance the tracer flux across the base of the mixed layer, via the formation of powerful small-scale fronts, even if the mixed layers become shallower due to enhanced restratification (Balwada et al. 2018).

The channel simulations considered here are representative of the Antarctic Circumpolar Current, and maybe to a smaller degree the separated western boundary currents. These are regions where deep isopycnals shoal to the surface, and the large-scale hydrography is conducive to exchanging tracers between the surface and deep ocean. Their role in being important sites for exchange across the mixed layer has long been known, as inferred from tracer distributions (Stommel 1979; Williams et al. 1995; Sallée et al. 2010; Marshall and Speer 2012). Our study speaks to the role of submesoscales in tracer dynamics of these regions, particularly in the winter when a strong density jump across the base of the mixed layer is not present. The impact of submesoscales in regions where isopycnals are relatively flat, or the isopycnals that reach into the interior are capped off by much lighter waters near the surface — an adiabatic surface-interior pathway is absent — is still relatively unknown and likely to be weak.

Our work has shown that statistical relationships between the surface kinematic properties and vertical exchange at depth exist. This suggests that the next-generation of satellite-based surface flow estimates, e.g. from SWOT (Morrow et al. 2019) or DopplerScatts (Rodríguez et al. 2018), can potentially help inform how climatically important tracers are being fluxed vertically and stored in the ocean. Some efforts in establishing dynamics based methods to reconstruct maps of vertical velocities are already underway (e.g. Qiu et al. 2020), and we suggest that statistical or machine learning approaches that directly infer the net fluxes will also be immensely fruitful.

APPENDIX A

Tracer gradient kinematics

Here we review of the fundamentals of the local kinematics of stirring in two dimensions; see Okubo (1970); Weiss (1991); Lapeyre et al. (1999); Majda (2003) for background. The analysis of two-dimensional flows in terms of the gradients of the velocity field (the strain tensor) is a fundamental tool with a long history, and the eigenvalues of the strain tensor can be used to understand the evolution of the gradient of a tracer advected by the flow.

The 2D tracer advection equation is

$$\frac{\mathrm{d}c}{\mathrm{d}t} \doteq \partial_t c + \boldsymbol{u} \cdot \nabla c = 0, \tag{A1}$$

where $\boldsymbol{u} = (u, v)$ and $c = c(x, y, t)$. Taking the gradient of (A1) gives the vector equation for the evolution of the gradient,

$$\frac{\mathrm{d}\nabla c}{\mathrm{d}t} = -\Lambda \nabla c, \quad \text{where} \quad \Lambda = \begin{bmatrix} u_x & v_x \\ u_y & v_y \end{bmatrix} \tag{A2}$$

is the transpose strain tensor. We can consider this as a dynamical system for the tracer gradient in the Lagrangian frame, taking the first term Taylor expansion of the velocity $\boldsymbol{u} = \dot{\boldsymbol{x}} = \Lambda^{\mathrm{T}} \boldsymbol{x}$, where Λ is constant, evaluated at the parcel's center $\boldsymbol{x} = \mathbf{0}$.

The transpose strain tensor can also be expressed as

$$\Lambda = \frac{1}{2} \begin{bmatrix} \delta + \sigma_n & \sigma_s + \zeta \\ \sigma_s - \zeta & \delta - \sigma_n \end{bmatrix} \tag{A3}$$

where the definitions in (1) are used.

The eigenvalues of Λ are

$$\lambda_{\pm} = \frac{1}{2} \left(\delta \pm \sqrt{\Omega} \right), \quad \text{where} \quad \Omega = \sigma^2 - \zeta^2 \tag{A4}$$

is the Okubo-Weiss parameter (Okubo 1970; Weiss 1991). Also, the eigenvalues are related to the determinant of the strain tensor and the magnitudes of the vorticity, strain and divergence as,

$$\det(\Lambda) = \lambda_+\lambda_- = \delta^2 + \zeta^2 - \sigma^2 = \delta^2 - \Omega. \tag{A5}$$

As long as the eigenvalues are distinct, they have linearly-independent eigenvectors $\boldsymbol{v}_\pm$, and one can express the tracer gradient as a linear combination of the eigenvectors, giving the full solution

$$\nabla c = a_+(0)e^{-\lambda_+ t}\boldsymbol{v}_+ + a_-(0)e^{-\lambda_- t}\boldsymbol{v}_-, \tag{A6}$$

where $a_\pm(0)$ are determined by the initial conditions.

If $\Omega < 0$ (vorticity dominant) and $\delta = 0$, the eigenvalues are complex, and the gradients rotate. If $\Omega > 0$ (strain dominant) and $\delta = 0$, the eigenvalues are equal and opposite in sign, leading to contraction (growth) in the $\boldsymbol{v}_-$ direction and expansion (decay) in the $\boldsymbol{v}_+$ direction. Convergence (negative divergence, $\delta < 0$) along with $\Omega > 0$ increases the rate of contraction, and possibly even makes both eigenvalues negative.

It is also instructive to compute the evolution equation for the squared gradient, which may be written

$$\frac{\mathrm{d}}{\mathrm{d}t}\frac{|\nabla c|^2}{2} = -\frac{\delta+\sigma}{2}c_\eta^2 - \frac{\delta-\sigma}{2}c_\xi^2, \tag{A7}$$

where (c_η, c_ξ) is the tracer gradient in the coordinate system defined by the two eigenvectors of the symmetric part of the strain tensor. This form shows directly that gradients grow when $\delta < 0$.

APPENDIX B

Joint distributions and conditional means

Consider a scalar field $F(x,y)$, along with the vorticity $\zeta(x,y)$ and the strain $\sigma(x,y)$, all defined on a control area A (the domain) at some z and t (for clarity we suppress these arguments below).

Then the quantity

$$\tilde{F}(\zeta,\sigma) \doteq \iint_A F(x,y)\delta[\zeta'(x,y)-\zeta]\,\delta[\sigma'(x,y)-\sigma]\,\mathrm{d}x\,\mathrm{d}y \tag{B1}$$

is the distribution of F conditioned on strain and vorticity. The spatial area integral of F and the integral over vorticity-strain space of $\tilde{F}$ have to be equal,

$$\iint_A F(x,y)\,\mathrm{d}x\,\mathrm{d}y = \iint_R \tilde{F}(\zeta',\sigma')\,\mathrm{d}\zeta'\,\mathrm{d}\sigma' \tag{B2}$$

where R is the range of vorticity and strain values found in spatial area A.

Notice that if $F=1$, and $\tilde{F}$ is defined on finite-difference grids, then $\tilde{F}(\zeta,\sigma)$ is the number of points in A with $\sigma' \in [\sigma, \sigma+\Delta\sigma)$ and $\zeta' \in [\zeta, \zeta+\Delta\zeta)$, divided by $\Delta\sigma\Delta\zeta$. Thus the total spatial area covered by points with strain and vorticity in this range is $\tilde{F}(\zeta,\sigma)\Delta\sigma\Delta\zeta\Delta x\Delta y$. The **joint probability distribution function (JPDF)** is correspondingly defined as,

$$P(\zeta,\sigma) = \frac{\tilde{F}(\zeta,\sigma)\Delta\sigma\Delta\zeta\Delta x\Delta y}{A}. \tag{B3}$$

The **spatial mean**, is defined as,

$$\overline{F} = \frac{\iint_A F(x,y)\,\mathrm{d}x\,\mathrm{d}y}{A}, \tag{B4}$$

while the **conditional mean** of F, always conditioned on surface vorticity and strain in this study, is defined as

$$\overline{F}^{\zeta\sigma}(\zeta,\sigma) = \frac{\iint F(x,y)\delta[\sigma'(x,y)-\sigma]\,\delta[\zeta'(x,y)-\zeta]\,\mathrm{d}x\,\mathrm{d}y}{\iint \delta[\sigma'(x,y)-\sigma]\,\delta[\zeta'(x,y)-\zeta]\,\mathrm{d}x\,\mathrm{d}y}. \tag{B5}$$

Note the difference in notation between the spatial and conditional means.

Acknowledgments. DB and ARG acknowledge support from the NSF grant OCE-1756882. KSS, RPA and QX acknowledge support from NASA award 80NSSC20K1142. This work would not have been possible without the tools provided by and maintained by the Pangeo community (`https://pangeo.io/`). The code for the analysis presented here is available at `https:`

//github.com/dhruvbalwada/vorticity-strain-conditioning, and most of the necessary data is at https://catalog.pangeo.io/browse/master/ocean/channel/, which allows the analysis to be done directly on the cloud (Abernathey et al. 2020).

References

Abernathey, R., and G. Haller, 2018: Transport by lagrangian vortices in the eastern pacific. *Journal of Physical Oceanography*, **48 (3)**, 667–685.

Abernathey, R., and Coauthors, 2020: Cloud-native repositories for big scientific data. *Authorea Preprints*.

Adams, K. A., P. Hosegood, J. R. Taylor, J.-B. Sallée, S. Bachman, R. Torres, and M. Stamper, 2017: Frontal circulation and submesoscale variability during the formation of a southern ocean mesoscale eddy. *Journal of Physical Oceanography*, **47 (7)**, 1737–1753.

Archer, M., A. Schaeffer, S. Keating, M. Roughan, R. Holmes, and L. Siegelman, 2020: Observations of submesoscale variability and frontal subduction within the mesoscale eddy field of the tasman sea. *Journal of Physical Oceanography*, **50 (5)**, 1509–1529.

Armi, L., and P. Flament, 1985: Cautionary remarks on the spectral interpretation of turbulent flows. *Journal of Geophysical Research: Oceans*, **90 (C6)**, 11 779–11 782.

Bachman, S. D., and A. Klocker, 2020: Interaction of jets and submesoscale dynamics leads to rapid ocean ventilation. *Journal of Physical Oceanography*, **50 (10)**, 2873–2883.

Balwada, D., K. S. Smith, and R. Abernathey, 2018: Submesoscale vertical velocities enhance tracer subduction in an idealized antarctic circumpolar current. *Geophysical Research Letters*, **45 (18)**, 9790–9802.

Barkan, R., M. J. Molemaker, K. Srinivasan, J. C. McWilliams, and E. A. DAsaro, 2019: The role of horizontal divergence in submesoscale frontogenesis. *Journal of Physical Oceanography*, **49 (6)**, 1593–1618.

Berta, M., and Coauthors, 2020: Submesoscale kinematic properties in summer and winter surface flows in the northern gulf of mexico. *Journal of Geophysical Research: Oceans*, **125 (10)**, e2020JC016 085.

Boccaletti, G., R. Ferrari, and B. Fox-Kemper, 2007: Mixed layer instabilities and restratification. *Journal of Physical Oceanography*, **37 (9)**, 2228–2250.

Brannigan, L., 2016: Intense submesoscale upwelling in anticyclonic eddies. *Geophysical Research Letters*, **43 (7)**, 3360–3369, doi:10.1002/2016GL067926.

Buckingham, C. E., J. Gula, and X. Carton, 2020a: The role of curvature in modifying frontal instabilities, part 1. *Journal of Physical Oceanography*.

Buckingham, C. E., J. Gula, and X. Carton, 2020b: The role of curvature in modifying frontal instabilities, part 2. *Journal of Physical Oceanography*, 1–67.

Callies, J., R. Barkan, and A. N. Garabato, 2020: Time scales of submesoscale flow inferred from a mooring array. *Journal of Physical Oceanography*, **50 (4)**, 1065–1086.

Callies, J., G. Flierl, R. Ferrari, and B. Fox-Kemper, 2016: The role of mixed-layer instabilities in submesoscale turbulence. *Journal of Fluid Mechanics*, **788**, 5–41.

Capet, X., J. C. McWilliams, M. J. Molemaker, and A. Shchepetkin, 2008: Mesoscale to submesoscale transition in the california current system. part ii: Frontal processes. *Journal of Physical Oceanography*, **38 (1)**, 44–64.

Ferrari, R., 2011: A frontal challenge for climate models. *Science*, **332 (6027)**, 316–317, doi: 10.1126/science.1203632.

Fox-Kemper, B., R. Ferrari, and R. Hallberg, 2008: Parameterization of mixed layer eddies. part i: Theory and diagnosis. *Journal of Physical Oceanography*, **38 (6)**, 1145–1165.

Franks, P. J., 2005: Plankton patchiness, turbulent transport and spatial spectra. *Marine Ecology Progress Series*, **294**, 295–309.

Freilich, M. A., and A. Mahadevan, 2019: Decomposition of vertical velocity for nutrient transport in the upper ocean. *Journal of Physical Oceanography*, **49 (6)**, 1561–1575.

Gula, J., M. J. Molemaker, and J. C. McWilliams, 2014: Submesoscale cold filaments in the gulf stream. *Journal of Physical Oceanography*, **44 (10)**, 2617–2643.

Haller, G., 2015: Lagrangian coherent structures. *Annual Review of Fluid Mechanics*, **47**, 137–162.

Hoskins, B., 1974: The role of potential vorticity in symmetric stability and instability. *Quarterly Journal of the Royal Meteorological Society*, **100 (425)**, 480–482.

Hoskins, B. J., and F. P. Bretherton, 1972: Atmospheric frontogenesis models: Mathematical formulation and solution. *Journal of the Atmospheric Sciences*, **29 (1)**, 11–37.

Klocker, A., 2018: Opening the window to the southern ocean: The role of jet dynamics. *Science advances*, **4 (10)**, eaao4719.

Lapeyre, G., and P. Klein, 2006: Dynamics of the upper oceanic layers in terms of surface quasi-geostrophy theory. *Journal of physical oceanography*, **36 (2)**, 165–176.

Lapeyre, G., P. Klein, and B. L. Hua, 1999: Does the tracer gradient vector align with the strain eigenvectors in 2D turbulence? *Physics of Fluids*, **11 (12)**, 3729–3737, doi:10.1063/1.870234.

Large, W. G., J. C. McWilliams, and S. C. Doney, 1994: Oceanic vertical mixing: A review and a model with a nonlocal boundary layer parameterization. *Reviews of Geophysics*, **32 (4)**, 363–403.

Lévy, M., P. J. S. Franks, and K. S. Smith, 2018: The role of submesoscale currents in structuring marine ecosystems. *Nature Communications*, **9 (1)**, 4758, doi:10.1038/s41467-018-07059-3.

Lévy, M., P. Klein, and A.-M. Treguier, 2001: Impact of sub-mesoscale physics on production and subduction of phytoplankton in an oligotrophic regime. *Journal of marine research*, **59 (4)**, 535–565.

Mahadevan, A., 2016: The impact of submesoscale physics on primary productivity of plankton. *Annual review of marine science*, **8**, 161–184.

Mahadevan, A., A. Pascual, D. L. Rudnick, S. Ruiz, J. Tintoré, and E. DAsaro, 2020: Coherent pathways for vertical transport from the surface ocean to interior. *Bulletin of the American Meteorological Society*, **101 (11)**, E1996–E2004.

Mahadevan, A., and A. Tandon, 2006: An analysis of mechanisms for submesoscale vertical motion at ocean fronts. *Ocean Modelling*, **14 (3-4)**, 241–256.

Majda, A. J., 2003: *Introduction to PDEs and Waves for the Atmosphere and Ocean*. American Mathematical Soc., 234 pp.

Marshall, D., 1997: Subduction of water masses in an eddying ocean. *Journal of Marine Research*, **55**, 201–222.

Marshall, J., and K. Speer, 2012: Closure of the meridional overturning circulation through southern ocean upwelling. *Nature Geoscience*, **5 (3)**, 171–180.

Marshall, J. C., R. G. Williams, and A. G. Nurser, 1993: Inferring the subduction rate and period over the north atlantic. *Journal of Physical Oceanography*, **23 (7)**, 1315–1329.

McWilliams, J. C., 2016: Submesoscale currents in the ocean. *Proceedings of the Royal Society A: Mathematical, Physical and Engineering Sciences*, **472 (2189)**, 20160 117.

Morrow, R., and Coauthors, 2019: Global observations of fine-scale ocean surface topography with the Surface Water and Ocean Topography (SWOT) mission. *Frontiers in Marine Science*, **6**, 232, doi:10.3389/fmars.2019.00232.

Okubo, A., 1970: Horizontal dispersion of floatable particles in the vicinity of velocity singularities such as convergences. *Deep-Sea Res.*, **17**, 445–454.

Olita, A., and Coauthors, 2017: Frontal dynamics boost primary production in the summer stratified mediterranean sea. *Ocean Dynamics*, **67 (6)**, 767–782.

Omand, M. M., E. A. DAsaro, C. M. Lee, M. J. Perry, N. Briggs, I. Cetinić, and A. Mahadevan, 2015: Eddy-driven subduction exports particulate organic carbon from the spring bloom. *Science*, **348 (6231)**, 222–225, doi:10.1126/science.1260062.

Price, J. F., R. A. Weller, and R. R. Schudlich, 1987: Wind-driven ocean currents and ekman transport. *Science*, **238 (4833)**, 1534–1538.

Qiu, B., S. Chen, P. Klein, H. Torres, J. Wang, L.-L. Fu, and D. Menemenlis, 2020: Reconstructing upper-ocean vertical velocity field from sea surface height in the presence of unbalanced motion. *Journal of Physical Oceanography*, **50 (1)**, 55–79.

Ramachandran, S., A. Tandon, and A. Mahadevan, 2014: Enhancement in vertical fluxes at a front by mesoscale-submesoscale coupling. *Journal of Geophysical Research: Oceans*, **119 (12)**, 8495–8511.

Rocha, C. B., S. T. Gille, T. K. Chereskin, and D. Menemenlis, 2016: Seasonality of submesoscale dynamics in the kuroshio extension. *Geophysical Research Letters*, **43 (21)**, 11–304.

Rodríguez, E., A. Wineteer, D. Perkovic-Martin, T. Gál, B. W. Stiles, N. Niamsuwan, and R. Rodriguez Monje, 2018: Estimating ocean vector winds and currents using a ka-band pencil-beam doppler scatterometer. *Remote Sensing*, **10 (4)**, 576.

Roullet, G., J. C. Mcwilliams, X. Capet, and M. J. Molemaker, 2012: Properties of steady geostrophic turbulence with isopycnal outcropping. *Journal of Physical Oceanography*, **42 (1)**, 18–38.

Ruiz, S., and Coauthors, 2019: Effects of oceanic mesoscale and submesoscale frontal processes on the vertical transport of phytoplankton. *Journal of Geophysical Research: Oceans*, **124 (8)**, 5999–6014.

Sallée, J.-B., K. Speer, S. Rintoul, and S. Wijffels, 2010: Southern ocean thermocline ventilation. *Journal of Physical Oceanography*, **40 (3)**, 509–529.

Shakespeare, C., 2015: On the generation of waves during frontogenesis. Ph.D. thesis, University of Cambridge.

Shcherbina, A. Y., E. A. D'Asaro, C. M. Lee, J. M. Klymak, M. J. Molemaker, and J. C. McWilliams, 2013: Statistics of vertical vorticity, divergence, and strain in a developed submesoscale turbulence field. *Geophysical Research Letters*, **40 (17)**, 4706–4711.

Siegelman, L., P. Klein, P. Rivière, A. F. Thompson, H. S. Torres, M. Flexas, and D. Menemenlis, 2020: Enhanced upward heat transport at deep submesoscale ocean fronts. *Nature Geoscience*, **13 (1)**, 50–55.

Sinha, A., D. Balwada, N. Tarshish, and R. Abernathey, 2019: Modulation of lateral transport by submesoscale flows and inertia-gravity waves. *Journal of Advances in Modeling Earth Systems*, **11 (4)**, 1039–1065.

Smith, K. M., P. E. Hamlington, and B. Fox-Kemper, 2016: Effects of submesoscale turbulence on ocean tracers. *Journal of Geophysical Research: Oceans*, **121 (1)**, 908–933.

Stommel, H., 1979: Determination of water mass properties of water pumped down from the ekman layer to the geostrophic flow below. *Proceedings of the National Academy of Sciences*, **76 (7)**, 3051–3055.

Su, Z., J. Wang, P. Klein, A. F. Thompson, and D. Menemenlis, 2018: Ocean submesoscales as a key component of the global heat budget. *Nature communications*, **9 (1)**, 1–8.

Theisel, H., 1995: Vector field curvature and applications. Ph.D. thesis, Verlag nicht ermittelbar.

Thomas, L. N., A. Tandon, and A. Mahadevan, 2008: Submesoscale processes and dynamics. *Ocean modeling in an Eddying Regime*, **177**, 17–38.

Uchida, T., D. Balwada, R. Abernathey, G. McKinley, S. Smith, and M. Lévy, 2019: The contribution of submesoscale over mesoscale eddy iron transport in the open southern ocean. *Journal of Advances in Modeling Earth Systems*, **11 (12)**, 3934–3958.

Uchida, T., D. Balwada, R. P. Abernathey, G. A. McKinley, S. K. Smith, and M. Lévy, 2020: Vertical eddy iron fluxes support primary production in the open southern ocean. *Nature communications*, **11 (1)**, 1–8.

Weiss, J., 1991: The dynamics of enstrophy transfer in two-dimensional hydrodynamics. *Physica D*, **48**, 273–294.

Williams, R. G., J. C. Marshall, and M. A. Spall, 1995: Does stommel's mixed layer demon work? *Journal of Physical Oceanography*, **25 (12)**, 3089–3102.

Zhang, W., C. L. Wolfe, and R. Abernathey, 2019: Role of coherent eddies in potential vorticity transport in two-layer quasigeostrophic turbulence. *arXiv preprint arXiv:1911.01520*.

LIST OF TABLES

	1 km					5 km	20 km
	Full	in 5 km simulation	in 20 km simulation	in 5 km coarsened	in 20 km coarsened	Full	Full
Front	60.4	59.7	47.6	59.8	53.4	60.4	61.8
Anticyclone	26.3	26.1	26	26.1	23.9	23.9	20
Cyclone	13.3	13	9.7	13.2	11.4	15.7	18.2

TABLE 1. Physical space area fraction occupied by different categories of flow features at different resolutions. The area fractions in the 1 km simulations, which are covered by the JPDF of the 5 and 20 km simulation and the 5 and 20 km coarsened fields are also shown in additional columns under the 1 km column.

LIST OF FIGURES

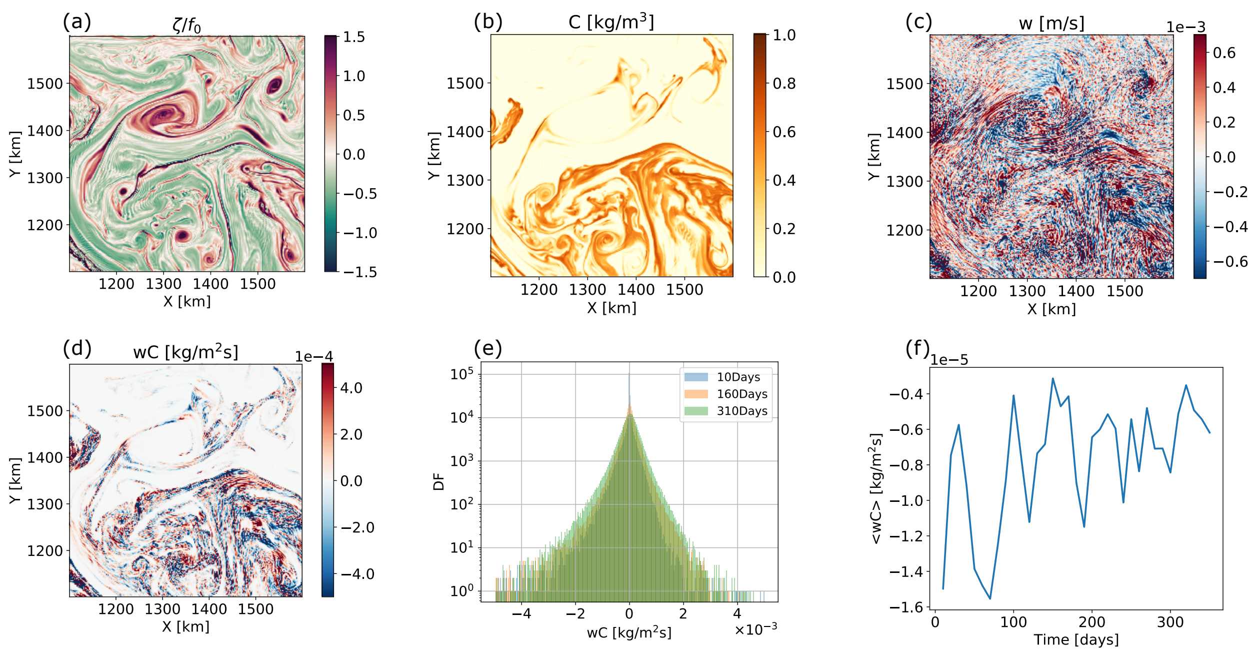

FIG. 1. The surface vorticity (a), tracer concentration (b), vertical velocity (c), and vertical tracer flux (d) at 100m depth 10 days after the tracer source is introduced at the surface in a small region upstream of the ridge. (e) Histogram of vertical flux in the chosen region at 3 different times. (f) Time series of the mean tracer flux in the chosen region. Notice that the mean tracer flux is almost two orders of magnitude smaller than the range of the instantaneous fluxes.

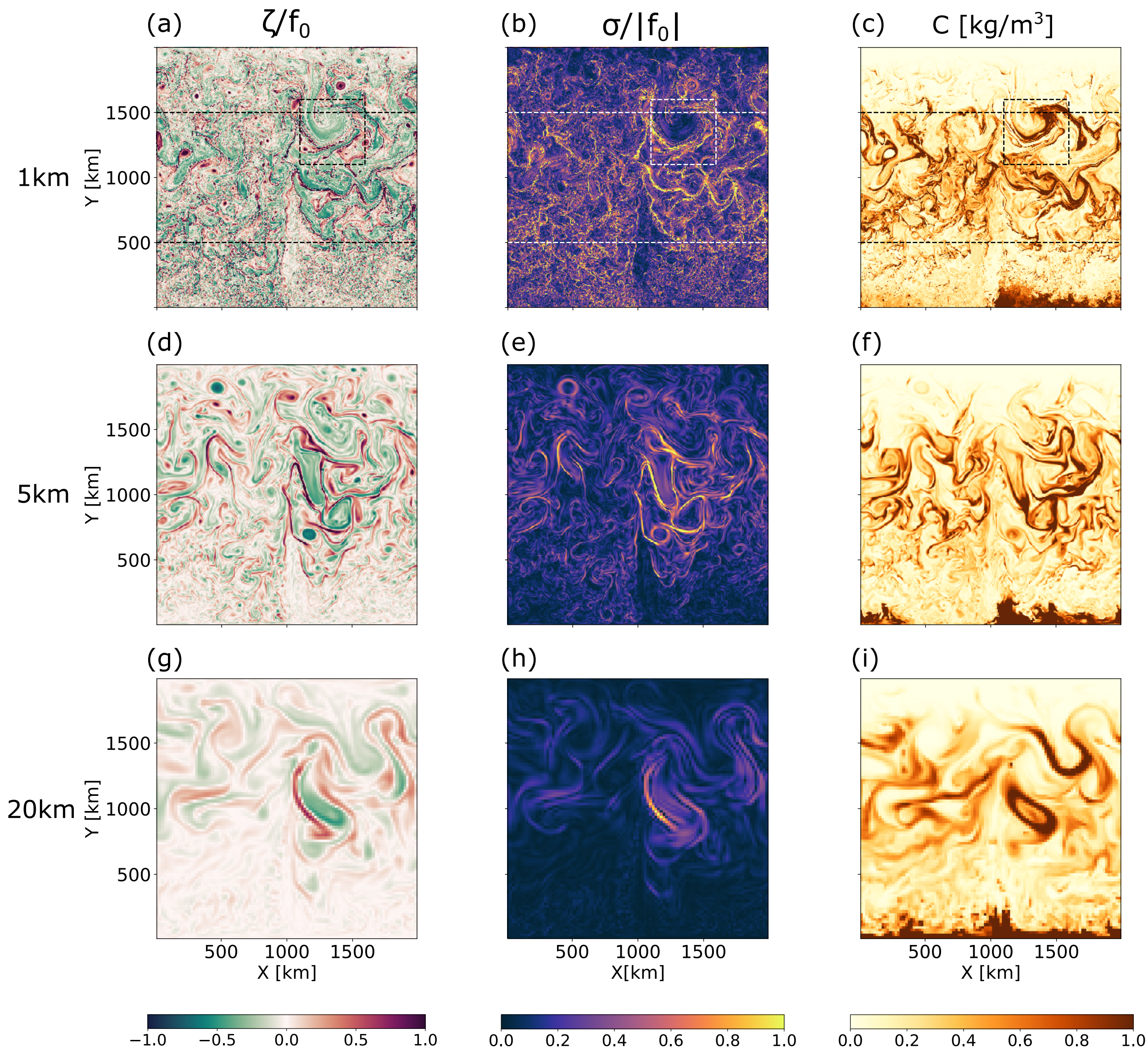

FIG. 2. Snapshot of surface vorticity (a,d,g), surface strain (b,e,h), tracer concentration at base of mixed layer (c,f,i) at 1 km (top row), 5 km (middle row) and 20 km (bottom row) resolutions. The vorticity and strain are normalized by the Coriolis frequency. The snapshot are taken 4 months after the tracer forcing is turned on. The horizontal dashed lines at 500 and 1500km in the upper left figure encompass the the analysis region used for most of the diagnostics in this study, and the dashed box upstream of the ridge indicates the region that is used for the fields in Figure 4.

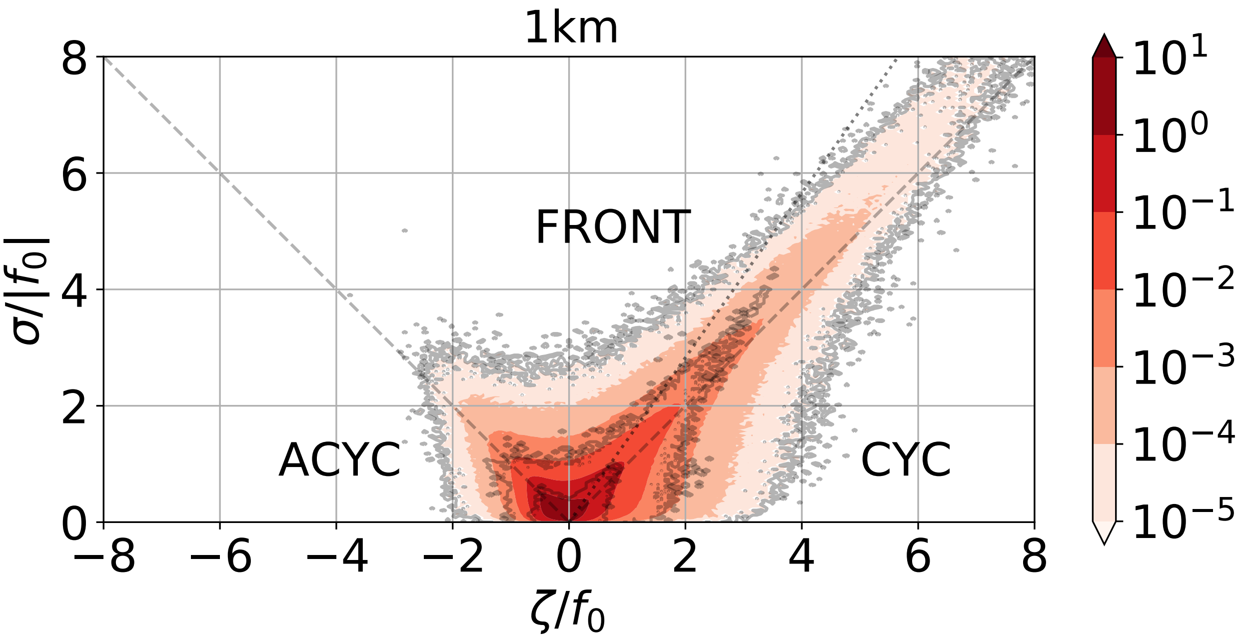

FIG. 3. Surface vorticity-strain JPDFs, for the 1 km simulation. The dashed lines correspond to the $\sigma = |\zeta|$, where the Okubo-Weiss parameter (Ω) is zero. The dotted line corresponds to the $\sigma = \sqrt{2}\zeta$. The gray contour lines in each of the panel correspond to the outer limits ($P(\zeta, \sigma) = 10^{-5}$) for the JPDFs from the 1 km, 5 km and 20 km simulations for comparison. We marked the regions that are associated with front, cyclone and anticyclone, where the demarcation is done based on the dashed lines.

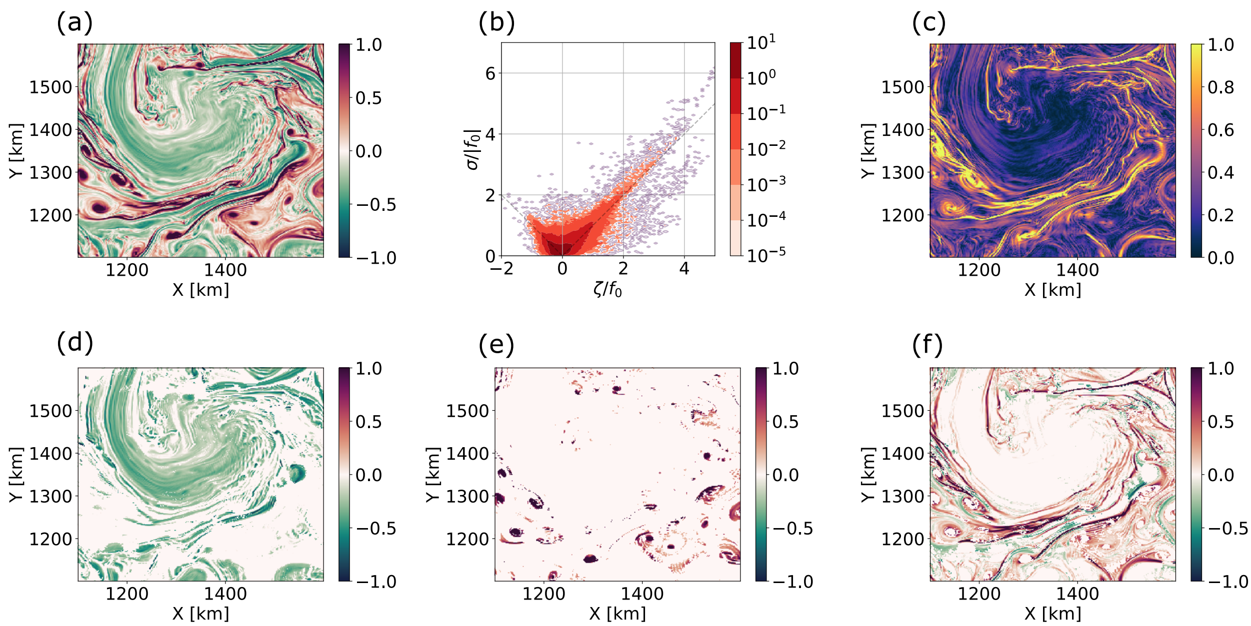

907 FIG. 4. vorticity-strain based flow feature decomposition. Surface vorticity (a) and surface strain (c) in a large scale anticyclonic meander downstream (box in Figure 2). (b) The JPDF corresponding to this region and snap shot. Bottom row shows the surface vorticity map decomposed based on where the grid points lie in the JPDF; corresponding to anticyclones (d), cyclones (e) and fronts (f).

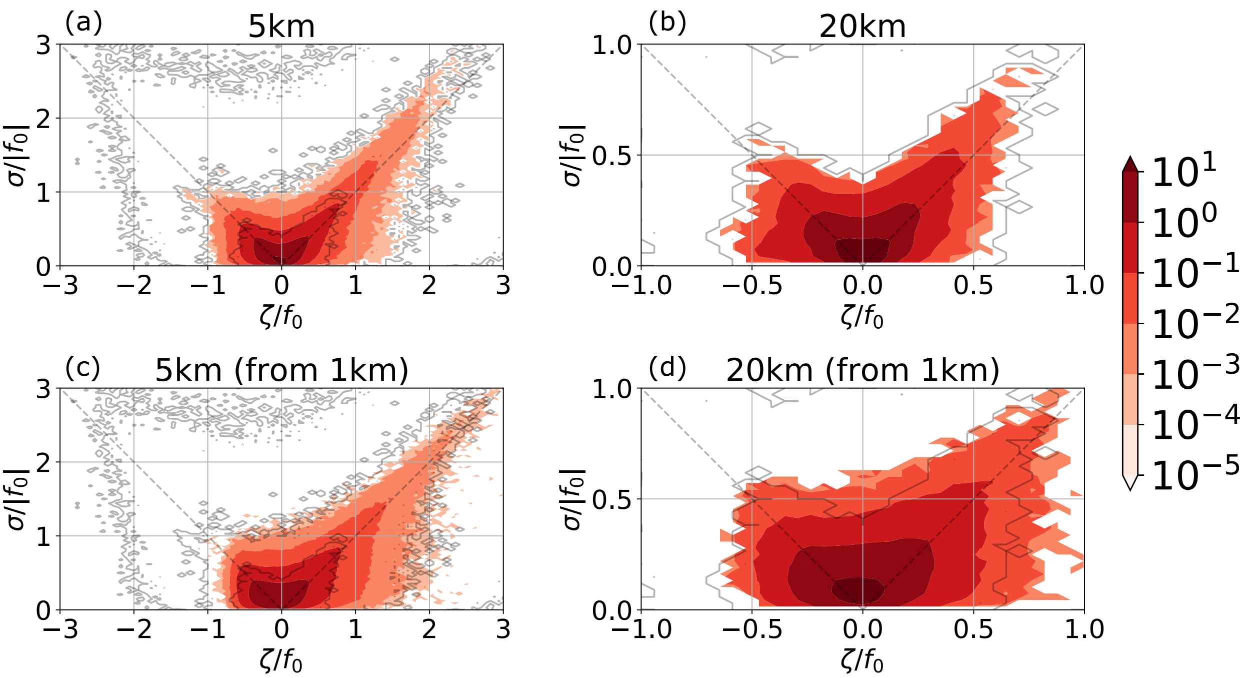

FIG. 5. Surface vorticity-strain JPDFs, for the (a) 5 km simulation, (b) 20 km simulation. (c,d) The vorticity-strain JPDFs of the coarse-grained velocities from the 1 km simulation, to 5 km and 20 km respectively. Contours and dashed lines are the same as in Figure 3.

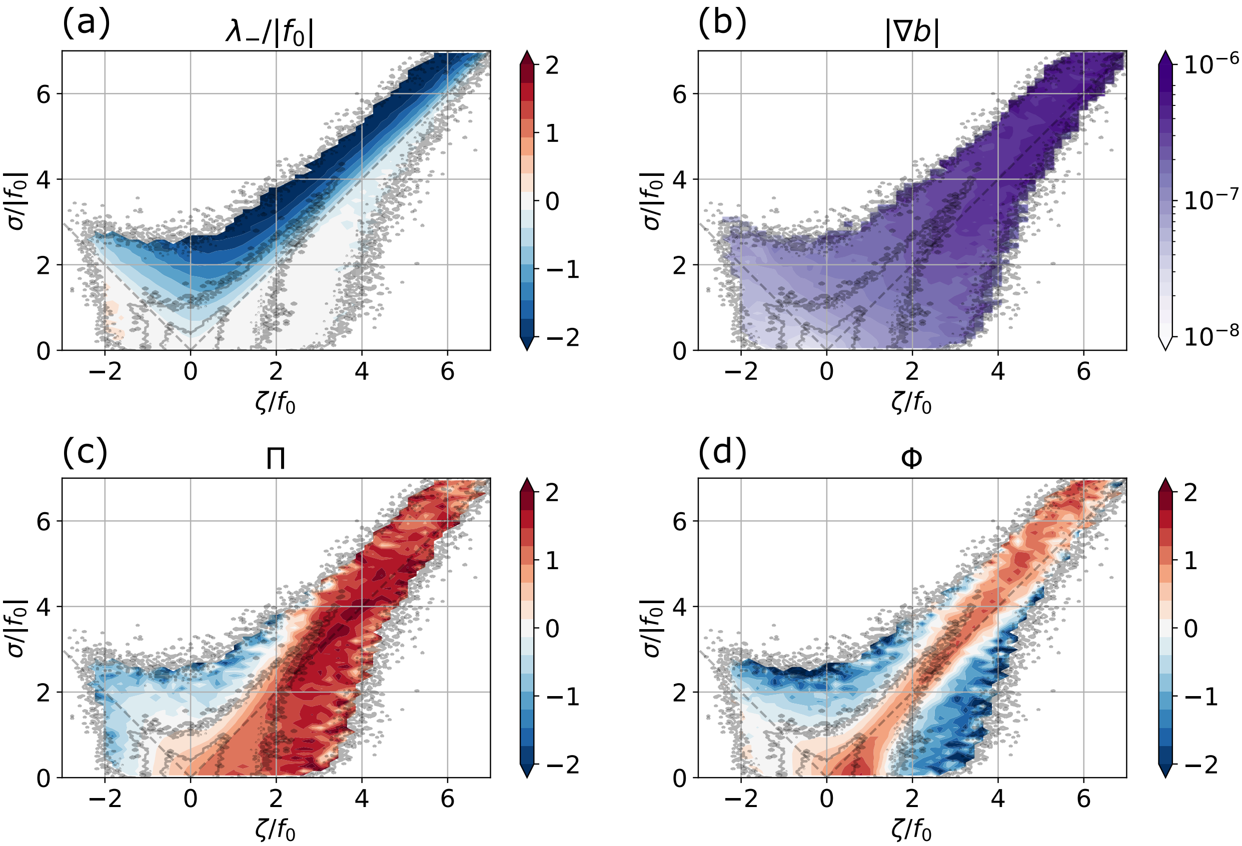

FIG. 6. Different criterion for instabilities and the strength of buoyancy gradients conditioned on vorticity-strain. The (a) conditional mean of the eigenvalue corresponding to rate of exponential growth of tracer gradients, where larger negative values correspond to more rapid increase in gradient; and (b) the conditional mean of the absolute buoyancy gradients. (c) the non-dimensionalized Ertel PV (Π), which shows the potential for gravitational, inertial and symmetric instabilities when it is negative; and (d) the generalized stability criterion from Buckingham et al. (2020a), which additionally considers the impact of flow curvature on instabilities and also suggests instabilities when it is negative. Contours and dashed lines are the same as in Figure 3.

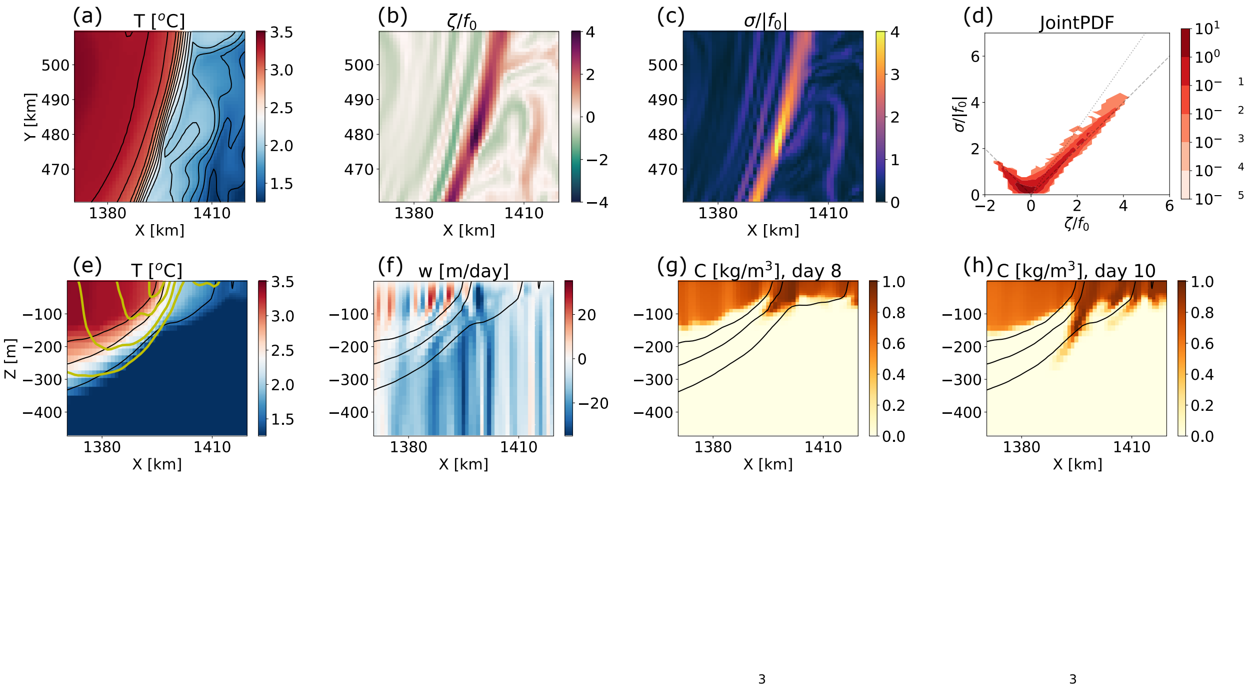

FIG. 7. Properties of a canonical front. The surface temperature (a), surface vorticity (b) and surface strain (c) in a region with a strong northward flowing front in it. (d) The vorticity-strain JPDF for the region. A depth-across front section of the temperature (e), vertical velocity (f), and tracer on day 8 (g) and 10 (h) after the tracer forcing is turned on. The black contours in (a, e, f, g, h) are some chosen temperature contours to highlight the front. The green contours in (e) show the meridional velocity, which is northwards, decaying away from the front.

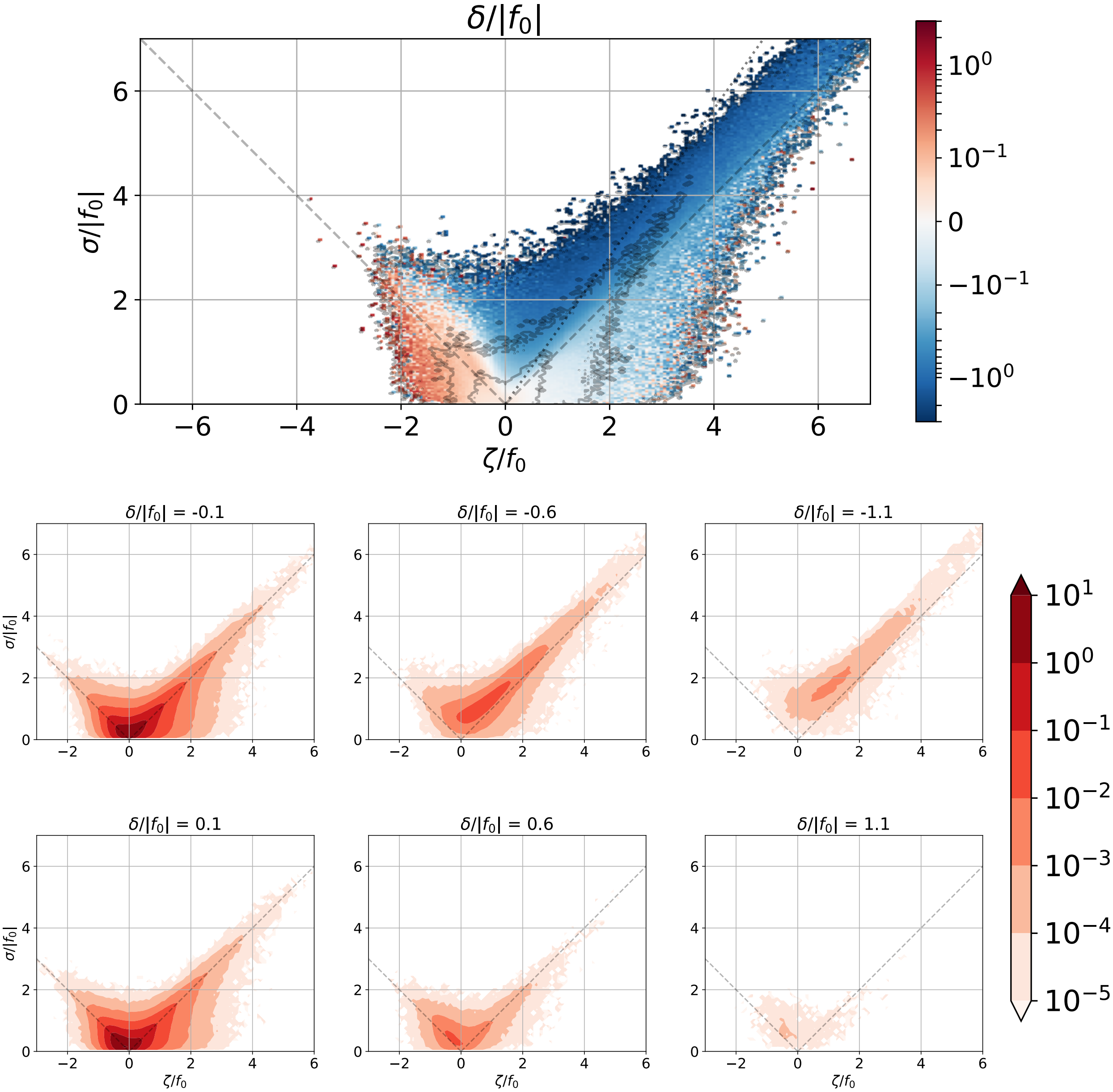

FIG. 8. Relationship of surface divergence to strain and vorticity. (a) The mean surface divergence conditioned on surface strain and vorticity. The light gray inner contour is the extent of the vorticity-strain JPDF for different resolutions as in Figure 3. (bottom two rows) The surface vorticity-strain JPDFs conditioned on different values of surface divergence; top row corresponds to convergent regions and bottom row to divergent regions. The dashed lines correspond to $\sigma = |\zeta|$.

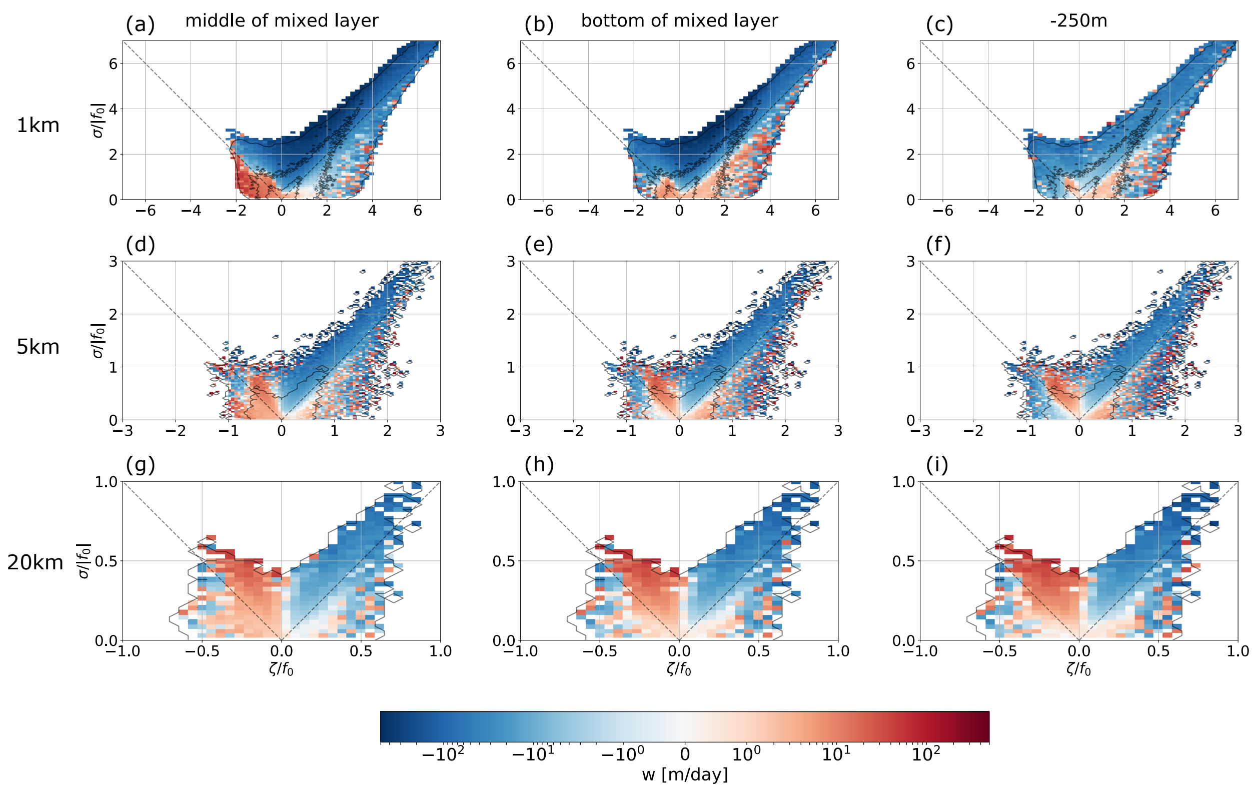

FIG. 9. Expected vertical velocity conditioned on the vorticity-strain JPDF at different resolutions (columns) and depths (rows). The top row is for 1 km resolution, followed by the 5 km and then the 20 km. The first column corresponds middle of the mixed layer (50m for 1 km, 75m for 5 km and 90m for 20 km), the second column to the base of the mixed layer (100m for 1 km, 150m for 5 km and 180m for 20 km), and the third column to a fixed depth of 250m. The dashed lines correspond to $\sigma = |\zeta|$.

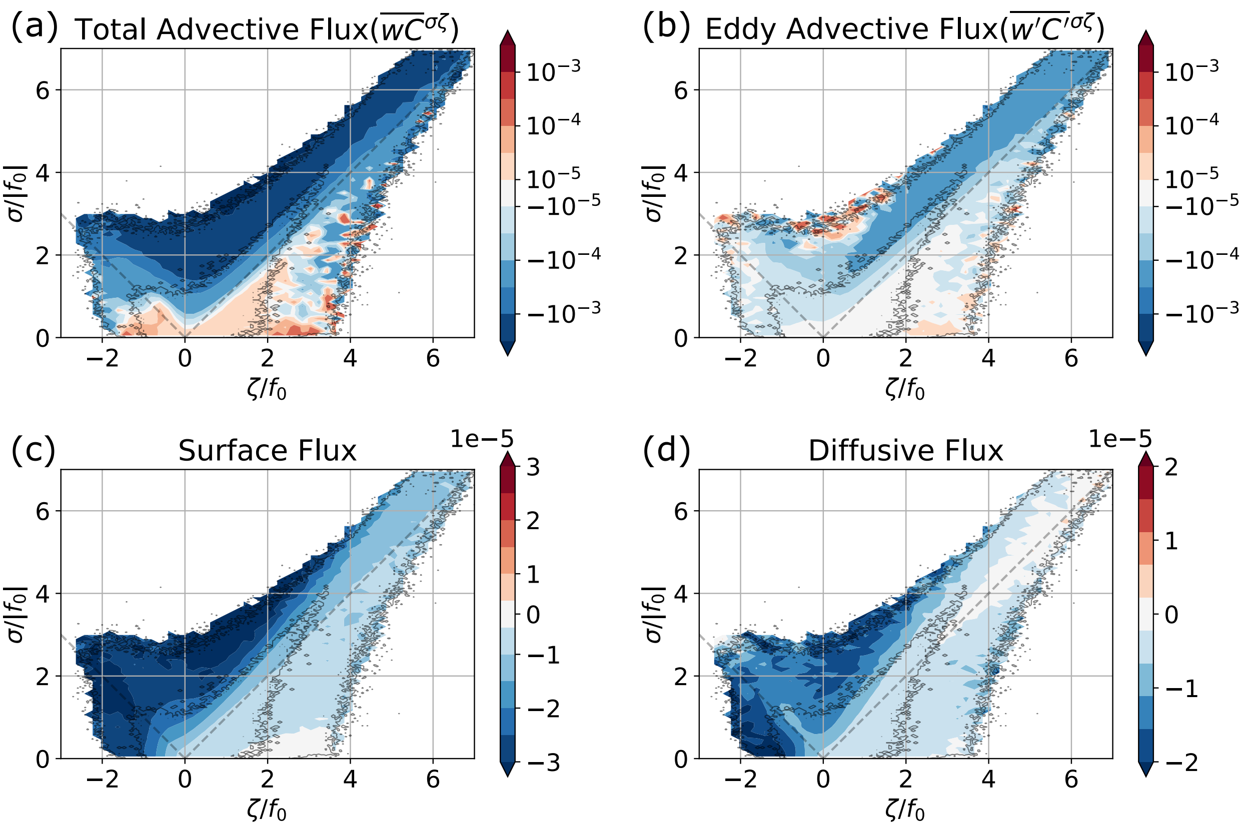

FIG. 10. Conditional mean of different components of the tracer flux conditioned on the surface strain and vorticity; the components being (a) the total advective flux, (b) the eddy advective flux, (c) the surface flux, and (d) the diffusive flux. Notice that the different panels are for different depths and have different color ranges. The diffusive flux is at the depth of 50m, which is the middle of the mixed layer — where the parameterized boundary layer diffusivity is the highest (not shown), and the advective fluxes are at the depth of 100m, which is the base of the mixed layer. The dashed lines correspond to $\sigma = |\zeta|$.

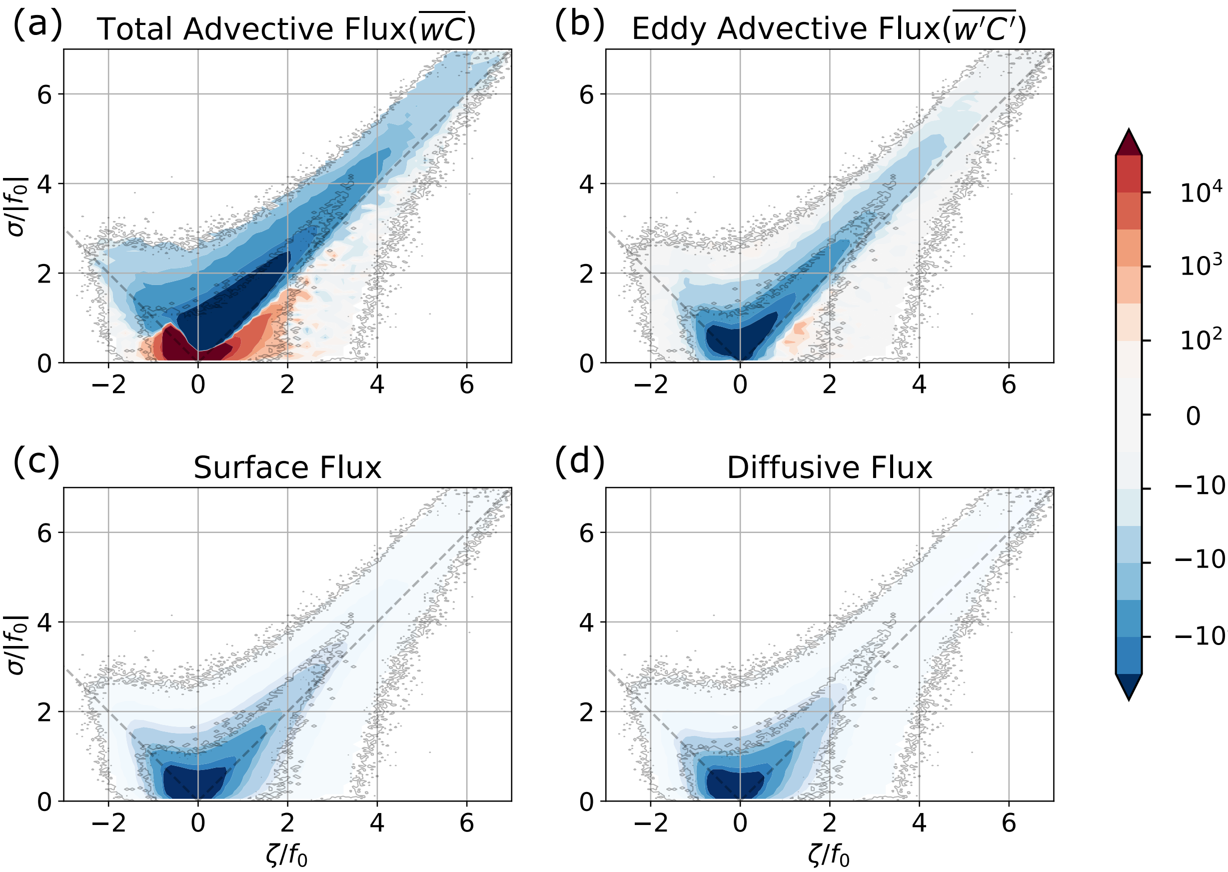

FIG. 11. The contribution of regions corresponding to different parts of the surface vorticity-strain JPDF to tracer transport for the different components of the flux — (a) total advective flux, (b) eddy advective flux, (c) surface flux, and (d) diffusive flux. The dashed lines correspond to $\sigma = |\zeta|$.

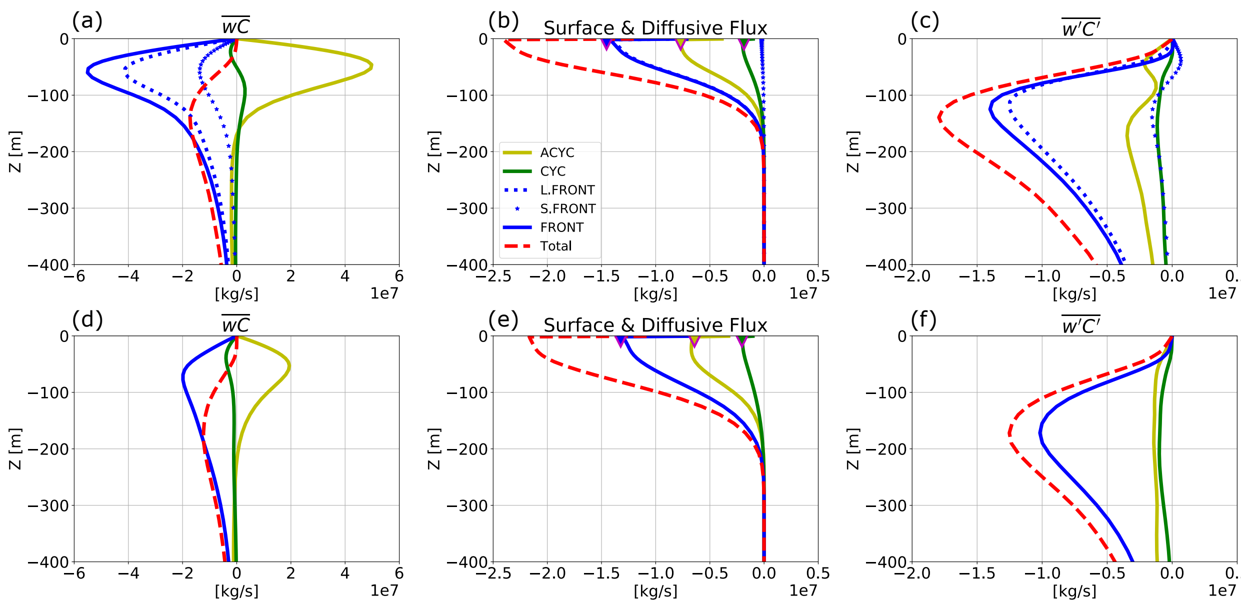

FIG. 12. Vertical structure of different tracer flux components in the 1 km (top row) and 5 km (bottom row) resolution simulations, separated into components based on the regions in the JPDF. The first column (a,d) shows the total advective flux (wC); the second column (b, e) shows the diffusive flux and the surface flux (inverted red triangles); and the third column (c, f) shows the eddy advective flux ($w'C'$) integrated over the parts of the JPDF corresponding to fronts (FRONT), cyclones (CYC) and anticyclones (ACYC). The sum of the parts is shown as the dashed red line. For the 1 km simulation we have divided contribution from the fronts into large front (L.FRONT) and small fronts (S.FRONT), where the small fronts is an integration over the part of the 1 km JPDF that is not covered by the 5 km JPDF.

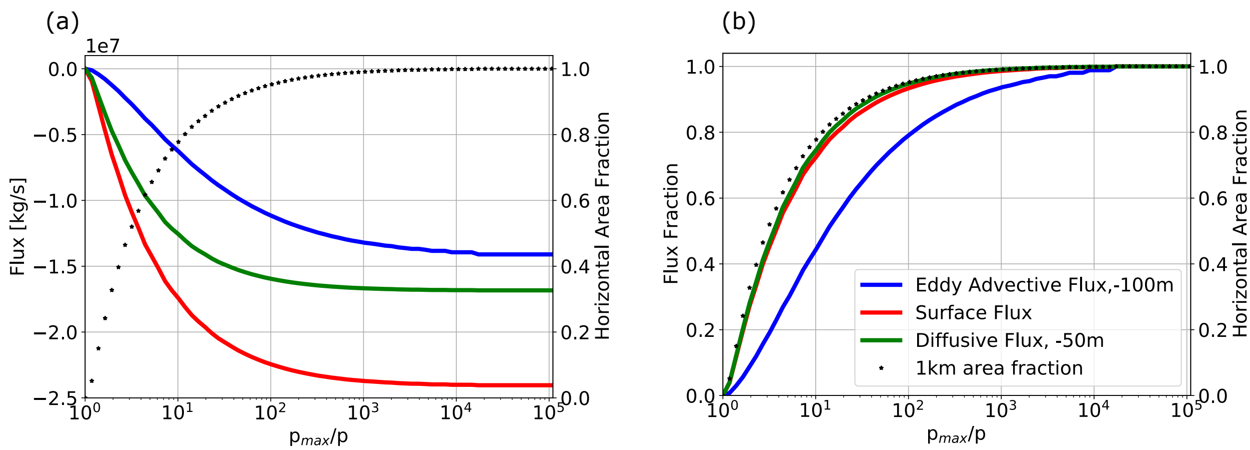

FIG. 13. Different flux components integrated outward from the origin ($\sigma = \zeta = 0$), where the maximum of the JPDF is present, to contours of decreasing probabilities (p) in the surface vorticity-strain JPDF. The integral is plotted as a function of $P_{\max}/P$, where P_{max} is the probability at the maximum of the JPDF. As shown in section 2d, higher values of $P_{\max}/P$ generally correspond to smaller-scale features. Each curve asymptotes to the respective total flux at the corresponding depth. (a) The eddy advective flux at 100 m, surface flux and diffusive fluxes at 50 m for the 1 km simulation. (b) The flux fraction, defined as the integrated flux divided by the total flux, for the different components shown in (a). The dotted black line (axis shown on right) corresponds to the spatial area fraction contained in the region corresponding to $P_{\max}/P$ for the 1 km simulation.

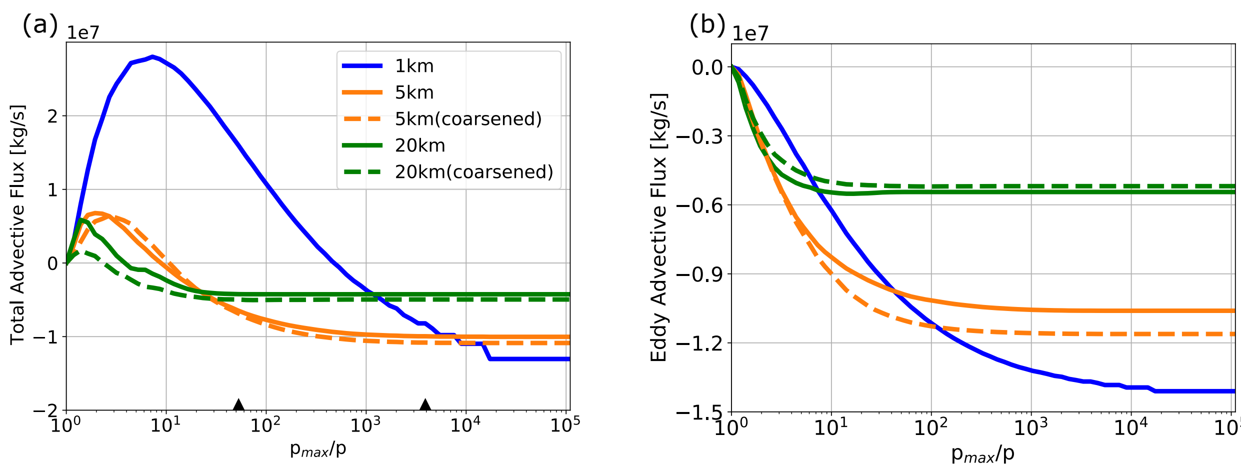

FIG. 14. The total advective flux (a) and the eddy advective flux (b) at the base of the mixed layer integrated outward from the origin as in Figure 13 for different resolutions and different coarsening scales applied to the 1 km simulation. Black markers at the bottom of (a) indicate outer-most probability contours of 20 km and 5 km simulations.